

Supporting information for

Advanced spectroscopy, microscopy, diffraction and thermal analysis of polyamide adhesives and prediction of their functional properties with solid-state NMR spectroscopy

Kash A. Bhullar¹, Aaron Meinel¹, Kennedy Maeder¹, Richard Wuhler², Marianne Gaborieau*¹, Patrice Castignolles¹

¹Western Sydney University, Australian Centre for Research on Separation Science (ACROSS), School of Science, Parramatta, 2150, Australia

²Western Sydney University, Advanced Materials Characterisation Facility (AMCF), Parramatta, 2150, Australia

Table of Contents

Table of Contents	1
S1. Sample preparation for X-ray diffraction and solid-state NMR	2
S2. Attenuated total reflection Fourier transform infrared	2
S3. Solid-state NMR spectroscopy	6
S3.1. Temperature calibration of MAS NMR probe.....	6
S3.2. ¹ H NMR.....	8
S3.3. ¹³ C SPE NMR	10
S3.3.1. Quantification.....	14
S3.3.2. Detection and quantification of Antistatic1	14
S3.3.3. Sensitivity.....	14
S3.4. ¹ H relaxation NMR.....	16
S3.4.1. T ₂ * data treatment.....	16
S3.4.2. T ₂ relaxation times.....	17
S3.4.3. T ₂ pre-exponential factors	19
S3.5. 2D-WISE NMR	20
S3.5.1. Optimization	20
S3.5.2. Measurements.....	28
S4. Scanning electron microscopy	33
S5. X-ray diffraction	35
S6. Thermogravimetric analysis	36
S7. Differential scanning calorimetry	37
S8. Mechanical and adhesive properties	39
References	42

S1. Sample preparation for X-ray diffraction and solid-state NMR

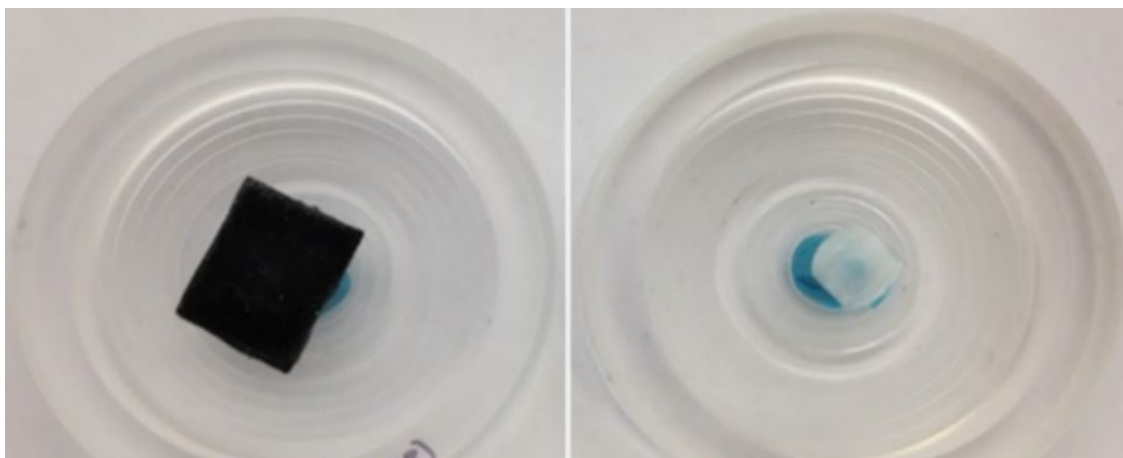


Figure S1: (left) HMA1 and (right) Antistatic1 samples on XRD sample holders on top of clay support (blue color)

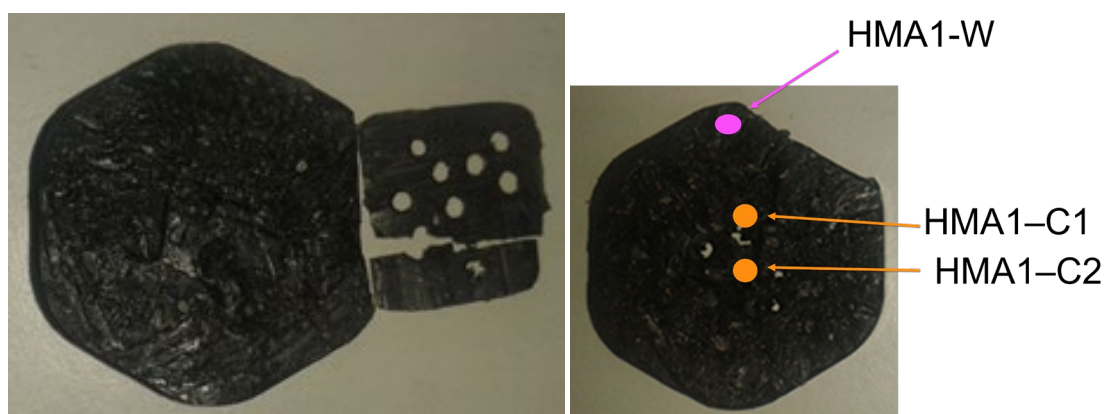


Figure S2: HMA1 pellet sliced, with punched holes.

S2. Attenuated total reflection Fourier transform infrared

All HMA samples were produced by extrusion. The potential contamination of HMA samples with PurgingAgent1 utilized during the extrusion process was investigated using ATR-FTIR spectroscopy. The ATR-FTIR spectra of all the HMA samples were compared with that of PurgingAgent1 (Figure 1). ATR-FTIR spectra of PurgingAgent1 revealed four main bands in the region between 2849 and 2916 cm^{-1} (CH_2 symmetric and asymmetric stretching vibrations), at 1471 cm^{-1} (C–H bending in CH_2), and 720 cm^{-1} (rocking mode of the CH_2). The signals were key identifiers of polyethylene.¹ Nevertheless,

due to the presence of the overlapping bands of the BaseResin1 and other additives in HMAs, it could not be concluded whether the HMA samples were contaminated with PurgingAgent1.

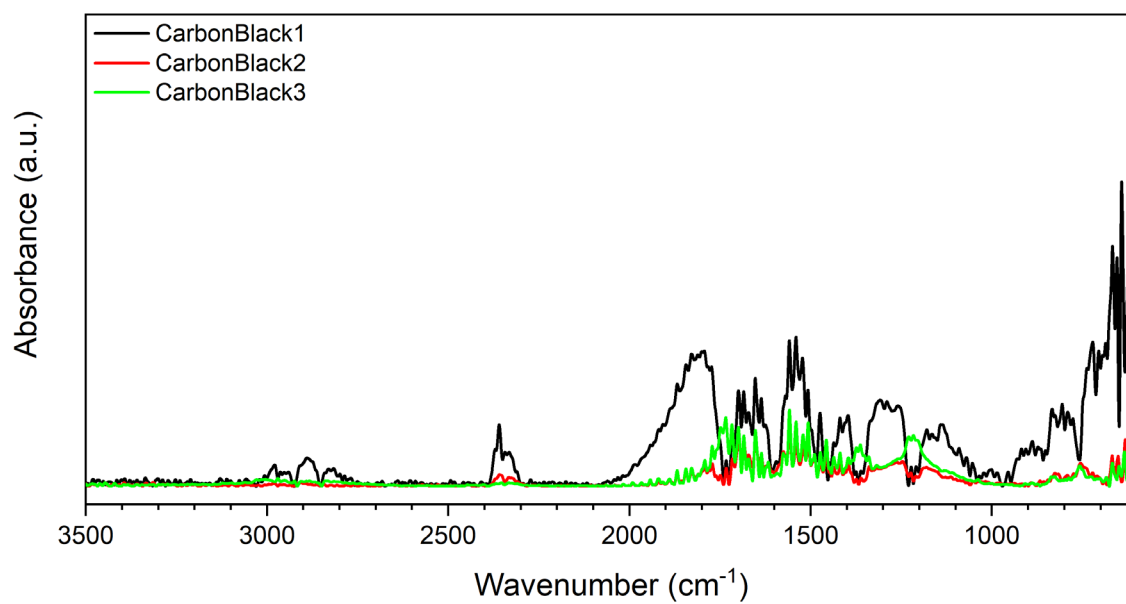


Figure S3: ATR-FTIR spectra of the three carbon black samples.

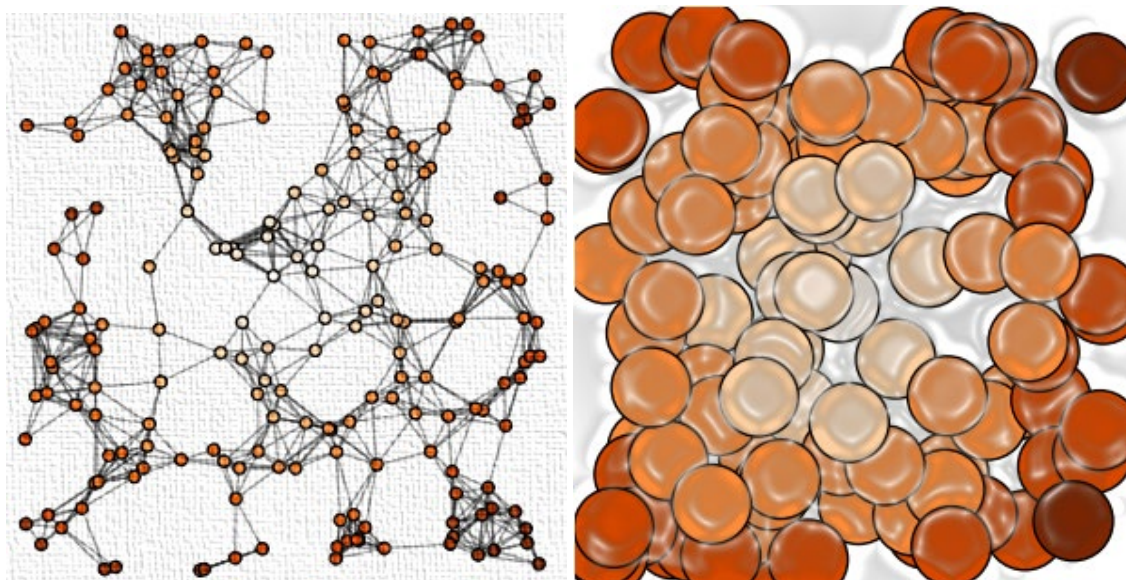


Figure S4: (Left) Schematic of percolation network, i.e., connected strings, and (right) system that does not percolate, i.e., aggregates.

S2. Attenuated total reflection Fourier transform infrared

Table S1: Band assignment for ATR-FTIR spectra of resin blends, their components, and the purging agent (in the 3600 - 600 cm^{-1} region) from Figure 1.

Wavenumber (cm^{-1})	Assignment	BaseResin1	Antiabrasion1	Antistatic1	Purging agent	HMA						
						1	2	3	4	5	6	7
3200-3600	O-H stretching ²	-	-	-	-	-	v	v	-	-	-	-
3250-3350	N-H (secondary amide), stretching ³	w	w	-	-	-	-	-	w	w	w	w
3000-3100	=C-H (trans-) stretching ³	v	v	-	-	-	-	-	-	-	-	-
2900-2950	-CH ₂ - (asymmetric stretching) ³	s	-	w	s	s	s	s	s	s	s	s
2800-2900	-CH ₂ - (symmetric stretching) ³	m	-	w	s	s	s	m	m	m	m	m
2400-2300	CO ₂ ⁴	v	v	v	-	-	w	w	v	w	v	-
1735	C=O stretching ⁵	v	-	-	-	-	-	-	-	-	-	-
1644	C=O (secondary amide, I) ⁶	m	v	-	-	s	-	-	s	s	s	s
1628	C=C ⁷	m	w	-	-	s	w	w	s	-	-	s
1611	C=C stretching vibration of aromatic ring ⁸	-	v	-	-	-	v	v	-	-	-	-
1575	C(O)-O ⁻⁷	w	-	-	-	-	-	-	-	-	m	-
1542	C-N (secondary amide, II) asymmetric deformation /CH ₂ ⁶	w	s	-	-	m	-	-	w	m	m	m
1512	C=C stretching vibration of aromatic ring ⁸	v	s	-	-	v	s	s	v	v	v	v
1500-1410	C-H bending in CH ₂ ¹	-	m	s	w	m	s	s	-	-	-	m

S2. Attenuated total reflection Fourier transform infrared

1464	N-H deformation/CH ₂ scissoring ⁶	w	m	v	-	m	m	m	m	m	m	m
1435	-C-H(<i>cis</i> -) bending (rocking) ³	w	w	v	-	m	-	v	m	m	m	m
1373	C(O)-O ⁻ or CN axial deformation ⁷ or CH ₂ wagging ⁶	v	w	v	-	w	m	w	w	w	w	w
1349	CH bend ⁹	v	w	-	-	v	m	v	v	v	v	v
1282	C-N (secondary amide, III) + C=O (carbonyl) asymmetric deformation ¹⁰	v	-	v	-	v	v	v	v	w	v	v
1243	C-N stretching ⁶	v	m	v	-	w	s	m	w	w	w	w
1219	C-N stretching ¹¹	v	m	w	-	w	m	m	w	w	w	w
1105	C-O (saturated aliphatic ether) ¹²	m	w	v	-	s	w	w	m	m	m	s
1013	C-C stretching ¹¹	w	v	-	-	w	v	v	w	w	w	w
930	CO-NH in plane ¹³	w	v	-	-	v	v	v	v	v	-	v
826	CH ₂ rocking ¹³ and C=C stretching vibration of aromatic ring ⁸	v	m	w	-	v	s	s	v	v	v	v
750-700	CH ₂ rocking mode ¹	-	v	-	w	w	w	w	-	-	-	w
722	-(CH ₂)- bending and -HC=CH- (<i>cis</i> -) ³	w	-	v		w	-	v	w	w	w	w

Key - v = very weak band, w = weak band, m = medium band and s = strong band

S3. Solid-state NMR spectroscopy

S3.1. Temperature calibration of MAS NMR probe

MAS NMR experiments at variable temperature (VT) are very useful to investigate and understand the structure and the dynamics of solid materials.¹⁴⁻¹⁷ The sample heating in our MAS VT-NMR probe is achieved by heating of the bearing gas. However, the temperature measured by the thermocouple in the NMR probe does not represent the actual sample temperature.¹⁸ The sample temperature is affected by the decompression of the bearing gas to atmospheric pressure, and by the friction between the surface of the rotor and the gas. These lead to sample cooling and heating, respectively, by unknown amounts.^{19, 20} The sample temperature is affected by radiofrequency heating, gas flow rate, bearing, gas temperature, and sample container material.¹⁸ Furthermore, the temperature can be non-uniform across the sample.²¹ The precise knowledge of the actual temperature inside the rotor is of utmost importance for temperature-dependent experiments utilizing MAS VT-NMR.

Several NMR thermometers have been developed to measure the actual sample temperature (T_{sample}) and temperature measured by the NMR probe thermocouple (T_{app}). The thermometers function via the observation of temperature-dependent chemical shifts, for example in ^{13}C NMR of samarium acetate,²² ^{31}P NMR of $(\text{VO})_2\text{P}_2\text{O}_5$,²³ ^{119}Sn NMR of $\text{Ln}_2\text{Sn}_2\text{O}_7$ ($\text{Ln} = \text{Pr, Vd, Sm, Eu, Tm, and Yb}$),²⁴ along with the most utilized ^{207}Pb NMR of $\text{Pb}(\text{NO}_3)_2$.²⁵⁻²⁸ The isotropic chemical shift δ_{iso} of $\text{Pb}(\text{NO}_3)_2$ varies linearly with the sample temperature at a rate of 0.70-0.775 ppm·K⁻¹ in the temperature range of ~200 K to 400 K. As a reference, the isotropic chemical shift of ^{207}Pb was measured in this work at room temperature after overnight equilibration with no gas flow (e.g., static conditions), therefore, it could be assumed that $T_{\text{sample}} = T_{\text{app}}$. In these conditions, the ^{207}Pb NMR chemical shift δ was measured, and Eq. S1 was used to calibrate the chemical shift scale of the acquired static spectrum of $\text{Pb}(\text{NO}_3)_2$.²⁷

$$\delta_{\text{peak}}(T) = -3670.6 + 0.666 \cdot T_{\text{sample}} \quad \text{S1}$$

The chemical shift scale of all acquired ^{207}Pb NMR spectra was then calibrated with respect to the calibrated static ^{207}Pb NMR spectrum. In this study, $\text{Pb}(\text{NO}_3)_2$ was utilized to calibrate an NMR probe in the range of room temperature to 390.2 K at various MAS rates using Eq. S2.²⁷

$$\delta_{\text{iso}}(T) = -3713.6 + 0.758 \cdot T_{\text{sample}} \quad \text{S2}$$

Solid-state NMR spectra were recorded on a Bruker DPX200 spectrometer operating at Larmor frequencies of 200 MHz and 50 MHz for ^1H and ^{13}C , respectively. A commercial double-resonance probe supporting zirconia MAS rotors with a 4 mm outer diameter was used. The VT gas flow rate was

S3. Solid-state NMR spectroscopy

set to $800 \text{ dm}^3 \cdot \text{h}^{-1}$. The apparent temperature range was between 290.2 K (25 °C) and 390.2 K (117 °C), controlled within 0.2 K. ^{207}Pb NMR spectra were recorded at 1, 2, 3, 4, 6.5, 8, 10 and 12 kHz MAS every 10 K using a $4.2 \mu\text{s}$ 90° pulse, a 5 s repetition delay and 8 scans. The actual sample temperature T_{sample} at each spinning rate was determined using Eq. S2 and plotted against the thermocouple temperature T_{app} (Figure S5).

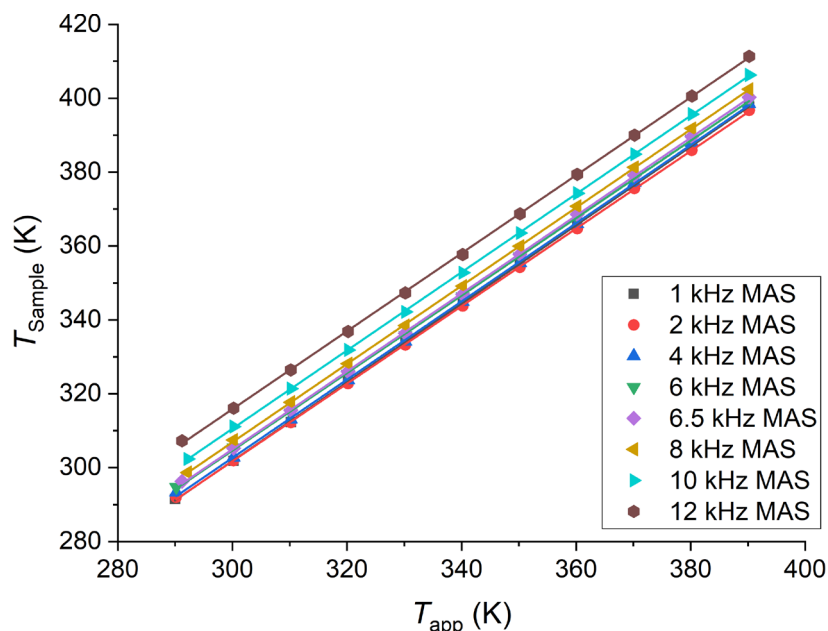


Figure S5: Sample temperature (T_{sample}) vs temperature measured by the NMR probe thermocouple (T_{app}) at different MAS rates. The lines represent linear fits.

Excellent linear correlations ($R^2 \geq 0.9998$) were observed between T_{sample} and T_{app} at each MAS rate. Intercepts and slopes of the linear fits are listed in Table S2.

Table S2: Summary data from Figure S5 T_{sample} vs T_{app} linear fits ($T_{\text{sample}} = m \cdot T_{\text{app}} + b$) with coefficient of determination (R^2).

MAS rate (kHz)	Slope	Intercept (K)	R^2
1	1.0637	-17.305	0.9999
2	1.0496	-13.165	0.9999
4	1.0582	-14.837	0.9998
6	1.0489	-10.106	0.9998
6.5	1.0543	-11.372	0.9999
8	1.0583	-10.625	0.9999
10	1.0590	-7.1861	0.9999
12	1.0553	-0.7788	0.9998

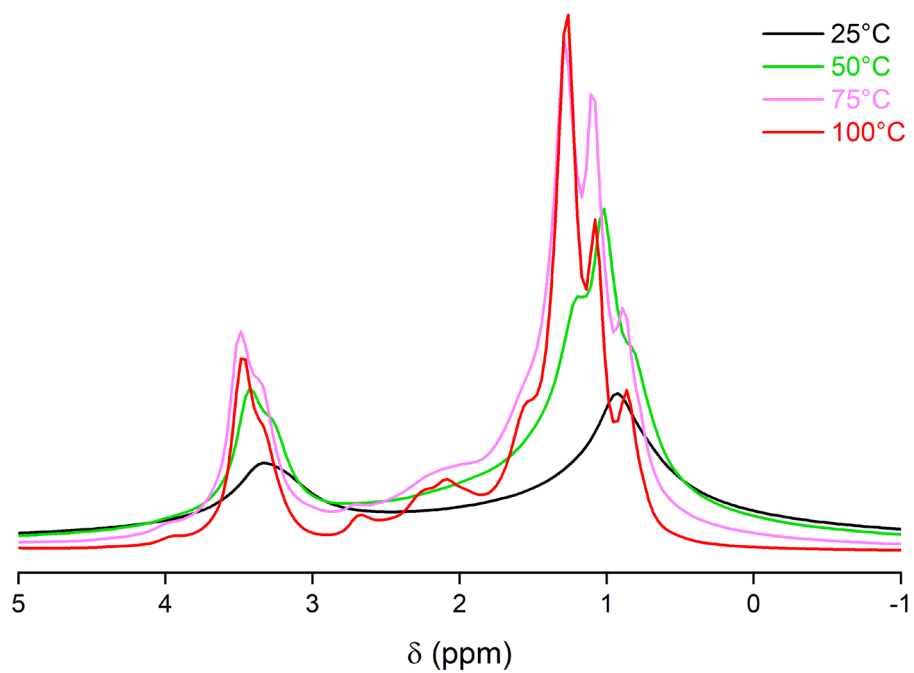
S3.2. ^1H NMR

Figure S6: Partial ^1H NMR spectra of BaseResin1 at 25, 50, 75, and 100 °C.

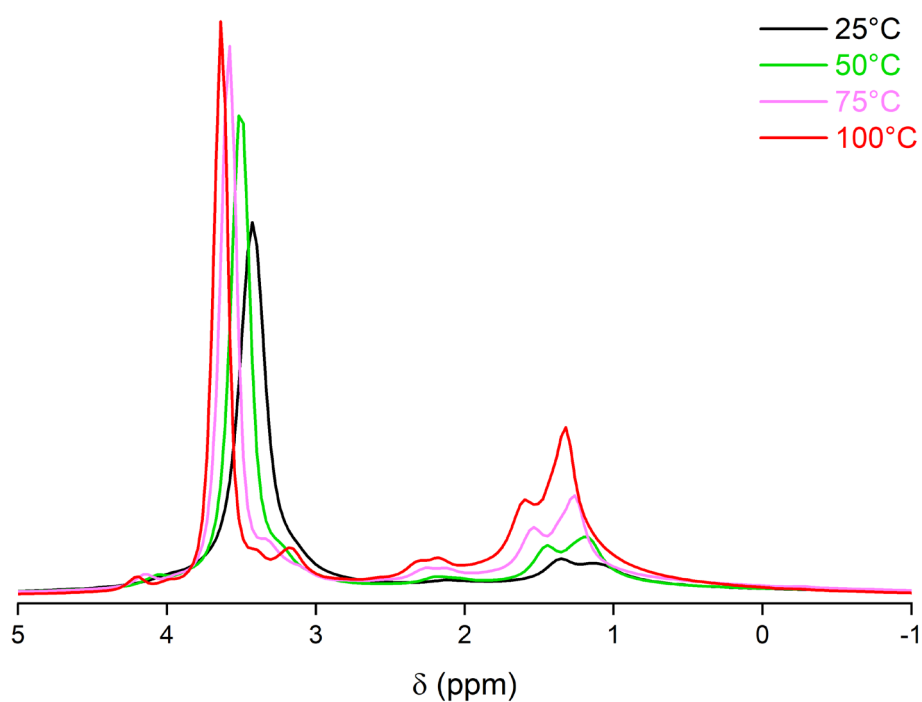


Figure S7: Partial ^1H NMR spectra of Antistatic1 at 25, 50, 75, and 100 °C.

S3. Solid-state NMR spectroscopy

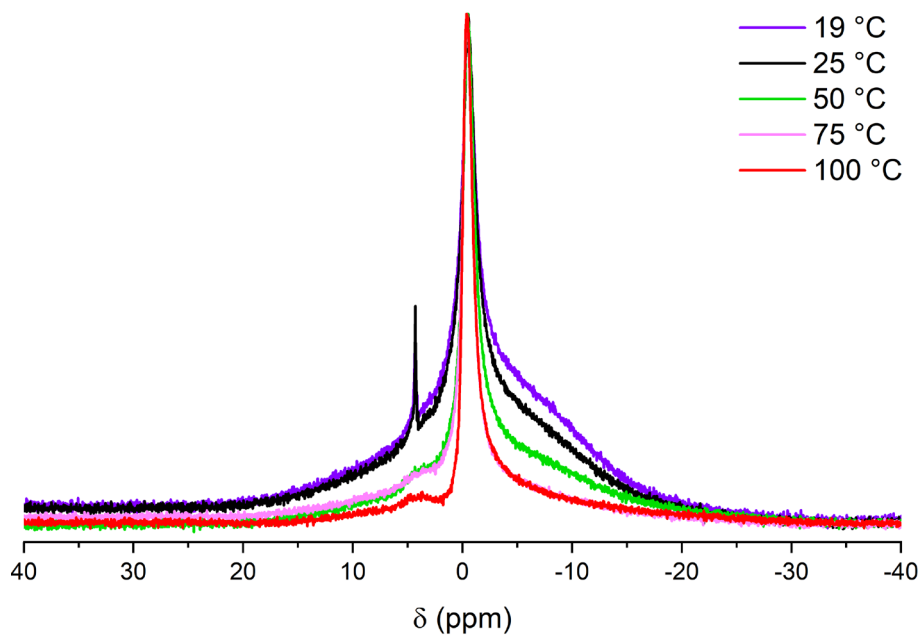


Figure S8: Partial ^1H NMR spectra of CarbonBlack1 at 19, 25, 50, 75, and 100 °C (normalized to the same intensity for the signal at 0 ppm).

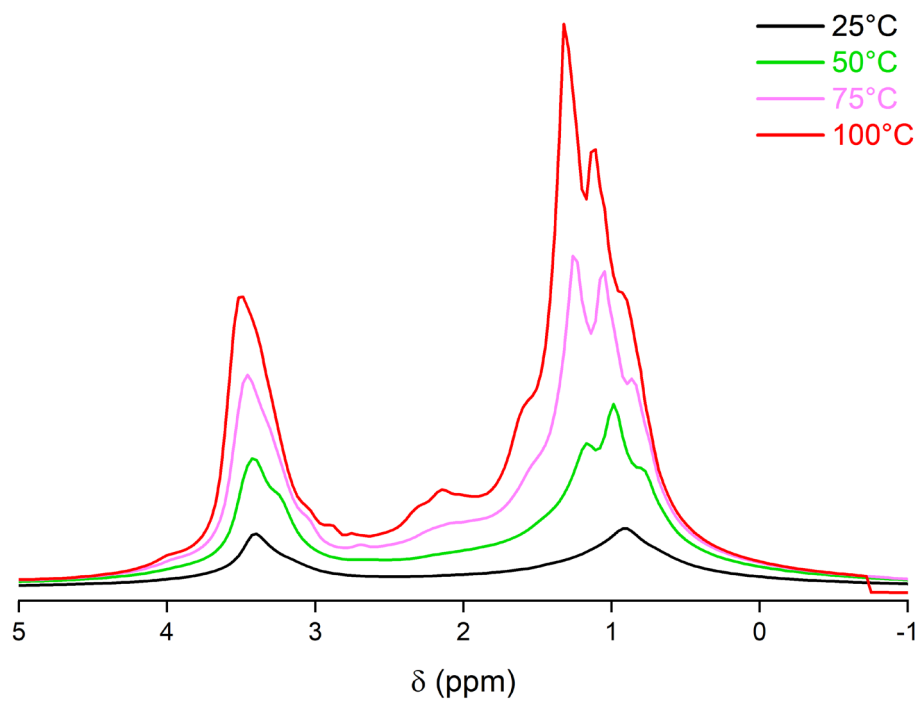


Figure S9: Partial ^1H NMR spectra of HMA1-C1 at 25, 50, 75, and 100 °C.

S3. Solid-state NMR spectroscopy

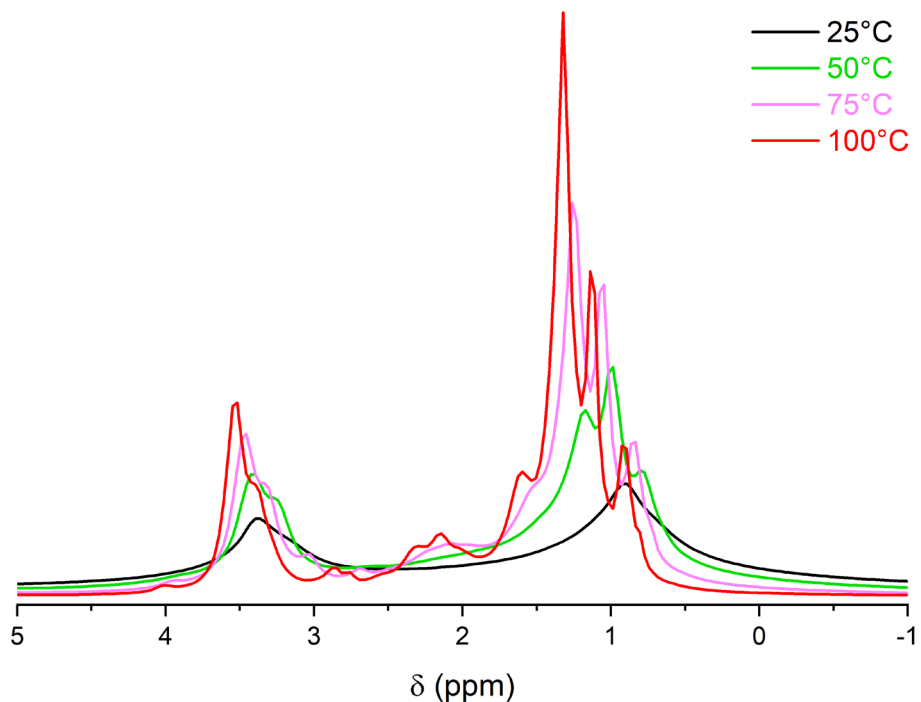


Figure S10: Partial ^1H NMR spectra of HMA1-W at 25, 50, 75, and 100 °C.

S3.3. ^{13}C SPE NMR

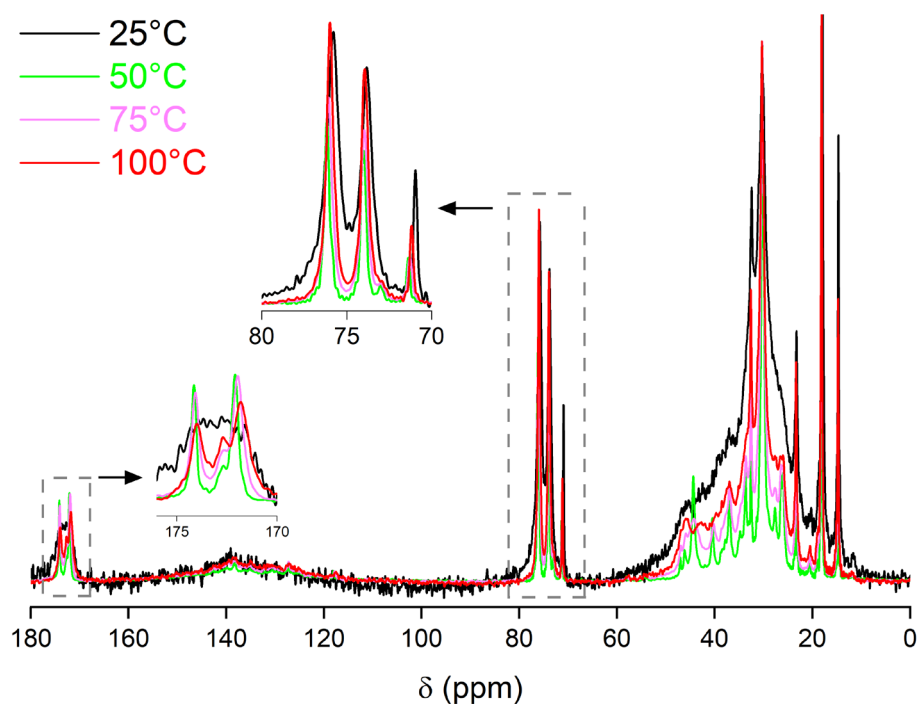


Figure S11: Partial ^{13}C SPE-MAS NMR spectra of HMA1-W at 25, 50, 75, and 100 °C (normalized to the same intensity for the signal at 30 ppm, see Table S3 for ^{13}C NMR signal assignment).

S3. Solid-state NMR spectroscopy

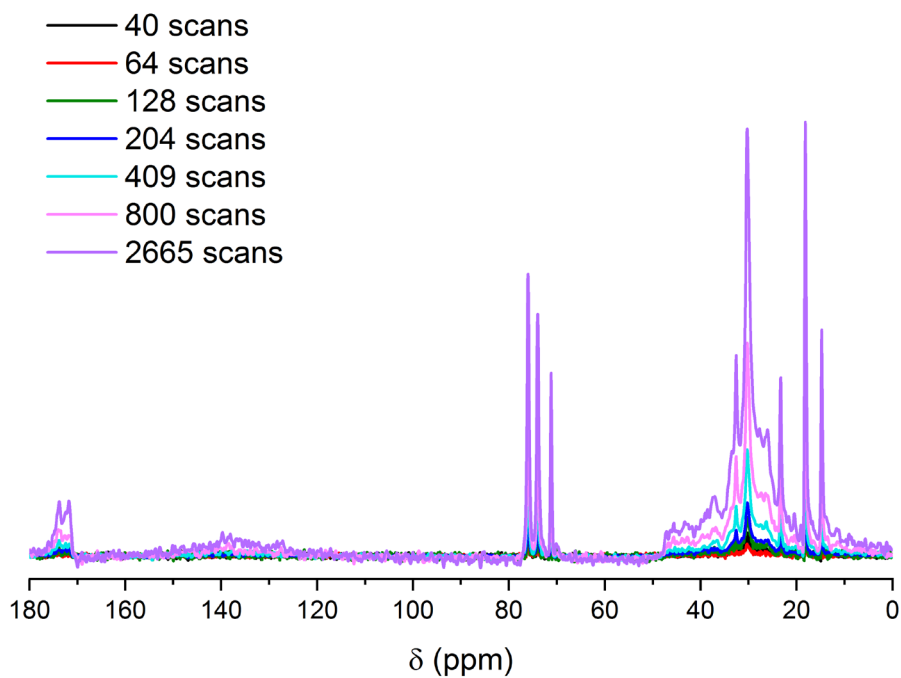


Figure S12: Quantitative ^{13}C NMR spectra of HMA1-C1 at 50 °C with different numbers of scans (not normalized, see Table S3 for ^{13}C NMR signal assignment).

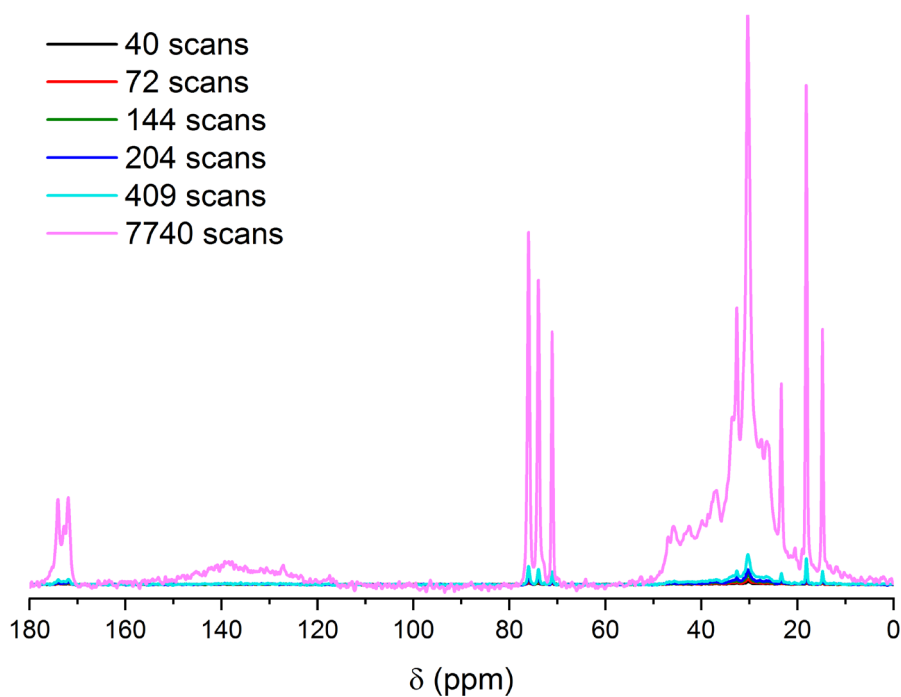


Figure S13: Quantitative ^{13}C NMR spectra of HMA1-C2 at 50 °C with different numbers of scans (not normalized, see Table S3 for ^{13}C NMR signal assignment).

S3. Solid-state NMR spectroscopy

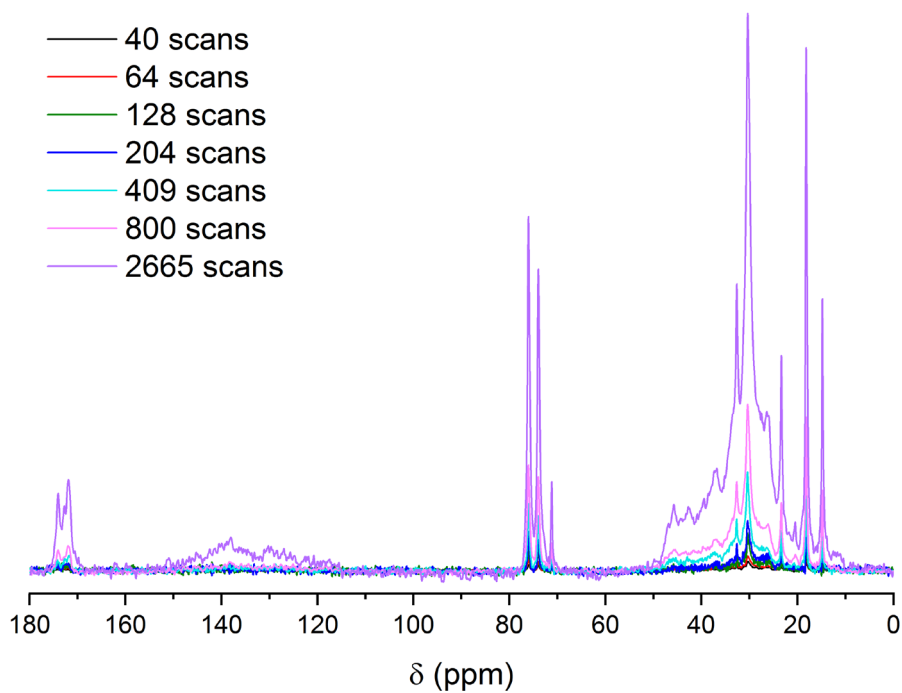


Figure S14: Quantitative ^{13}C NMR spectra of HMA1-W at 50 °C with different numbers of scans (not normalized, see Table S3 for ^{13}C NMR signal assignment).

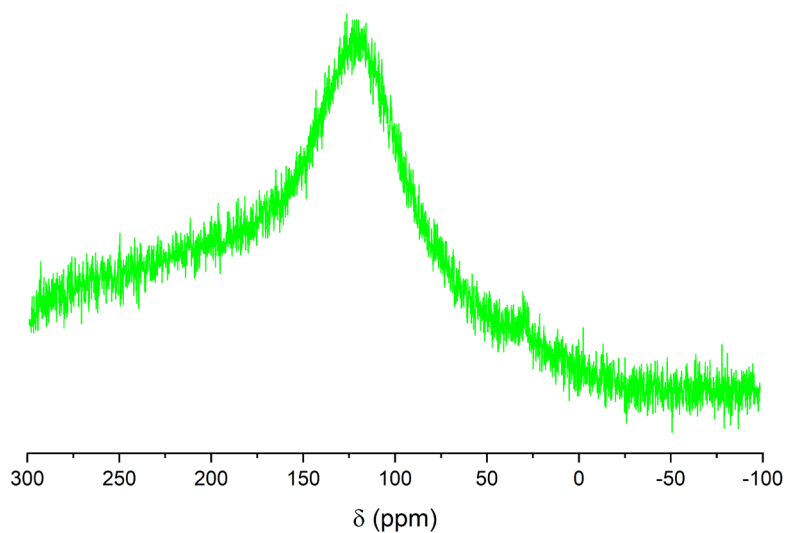


Figure S15: ^{13}C NMR spectrum of CarbonBlack1 acquired with a repetition delay of 60 s with 75980 scans at room temperature.

S3. Solid-state NMR spectroscopy

Table S3: Signal assignment of ^{13}C NMR spectra of BaseResin1, Antiabrasion1, Antistatic1, HMA1, HMA7 HMA1–C1, HMA1–C2, and HMA1–W along with chemical shift values observed (δ_{exp}), from literature (δ_{lit}) or simulated with ChemDraw (δ_{th}).

δ_{exp} (ppm)								Assignment	δ_{lit} (ppm)	δ_{th} (ppm)
BaseResin1	Antiabrasion1	Antistatic1	HMA1	HMA7	HMA1–C1	HMA1–C2	HMA1–W			
172.3	-	173.7	173.9	173.4	179.8	174.1	174.2	R-(CH ₂) _n - <u>C</u> (O)-OH	174-180 ²⁹⁻³¹	175-180
	-		171.8	172.4	171.8	171.9	172.1	R-(CH ₂) _n - <u>C</u> (O)-NH-R	171-175 ³⁰	170-175
-	167.3	-	-	-	-	-	-	R- <u>C</u> (O)-N(R) ₂	163-170 ³⁰	165-170
131.3-139.2	135.6	138	138.1	136.8-139.7	135.4-139.3	135.5-139.3	135.2-142.7	R ₂ CH-CH= <u>C</u> H-CHR ₂ (<i>cyclo</i> -) and aromatic	130-140 ^{30, 32, 33}	130-145
-	122.9, 127.7	-	117.9-127.1	120.7-128.3	121.7, 130.1	117.3-130.6	118.1-130.7	R ₂ C= <u>C</u> R ₂ (di-substituted) and aromatic	114-130 ^{30, 32, 33}	115-130
75.8	-	-	75.9	75.8	75.9	76.0	76.2	R-O- <u>CH</u> (CH ₃)-CH ₂ -O-R	75-77 ^{30, 32}	75-80
73.8	-	-	73.9	73.9	73.9	73.9	74.0	R-O-CH(CH ₃)- <u>CH</u> ₂ -O-R	70-74 ³²	70-75
-	-	69.5, 64	71.1	-	70.9	71.1	71.4	R-O- <u>CH</u> ₂ - <u>CH</u> ₂ -O-R	60 ³⁰	65-70
45.6	-	40.1	45.9	44.6	45.6	45.9	46.2	R- <u>CH</u> ₂ -NH-C(O)-R	40.3-43 ^{30, 31}	44-50
39.4	-	-	43.2	42.8	42.1	42.6	44.4, 40.5	R- <u>CH</u> ₂ -NH-C(O)-R, R- <u>CH</u> ₂ -NH ₂ , R ₂ CH- <u>CH</u> R ₂ (<i>cyclo</i> -)	38-42 ³⁰⁻³²	39-44
35.1	-	37.1	39.8	38.8	36.9	36.9	37.0	R-(CH ₂) _n - <u>CH</u> ₂ -C(O)-NH-R, R-(CH ₂) _n - <u>CH</u> ₂ -RC=CHR, R ₂ CH- <u>CH</u> ₂ -(CH ₂) _n -COOH	35.5 ^{30, 31}	36-39
-	-	33.3	37	36.9	-	33.5	33.7	R-CH=C(R)- <u>CH</u> ₂ -(CH ₂) _n -R, R ₂ CH-(CH ₂) _n - <u>CH</u> ₂ -COO-R, R-CH=C(R)- <u>CH</u> R-(CH ₂) _n -R	35.5 ^{30, 31}	33-36
32.5	-	-	32.6	32.4	32.5	32.6	32.6	R ₂ CH- <u>CH</u> ₂ -(CH ₂) _n -R	25-32 ^{30, 31}	33-34
30.3	-	30.2, 27.3	30.3	30.5	30.39	-	30.3, 27.7	R-(CH ₂) _n - <u>CH</u> ₂ -(CH ₂) _n -R	25-30 ^{30, 31}	25-33
-	-	-	26.4	26.5	-	26.4	26, 26.4	R- <u>CH</u> ₂ -CH ₂ -C(O)-NH-R, R-CH=CH- <u>CH</u> ₂ -CH=CH-R	22-25 ^{30, 31}	24-26
23.3	-	-	23.4	23.5	23.4	23.4	23.3, 23.6	CH ₃ - <u>CH</u> ₂ -(CH ₂) _n -R	22-23 ³⁰	20-23
-	-	-	-	-	20.3	20.5	20.5	<u>CH</u> ₃ -R	10-20 ³³	19-21
18.1	-	-	18.1	18.2	18.1	18.2	18.2	R-O-CH(<u>CH</u> ₃)-CH ₂ -O-R	16-19 ³²	15-19
14.7	-	-	14.8	14.8	14.8	14.8	14.7	R-(CH ₂) _n -CH ₂ - <u>CH</u> ₃	13.7 ³⁰	10-15

S3.3.1. Quantification

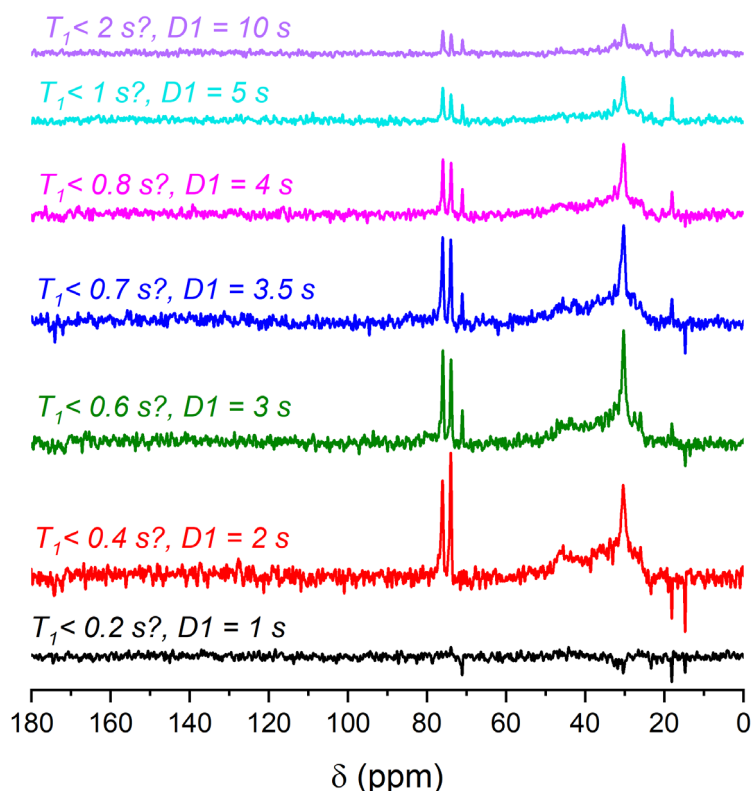


Figure S16: One-dimensional ^{13}C inversion recovery spectra for HMA1–C2, testing for different T_1 values at 50 °C (with different repetition delays D_1 , not normalized see Table S3 for ^{13}C NMR signal assignment).

S3.3.2. Detection and quantification of Antistatic1

Table S4: Summary of the antistatic quantification using ^{13}C NMR for HMA1, HMA1–C1, HMA1–C2 and HMA1–W.

Sample	F_{AS} (%)	SNR	RSD (%)	Standard deviation
HMA1	15.7	36.3	2.40	0.38
HMA1–C1	11.2	31.5	2.88	0.32
HMA1–C2	21.6	40.1	2.11	0.46
HMA1–W	5.6	15.2	7.31	0.41

S3.3.3. Sensitivity

The quantitative ^{13}C measurements of HMA1–C1, HMA1–C2, and HMA1–W showed as expected that the SNR of the 71 ppm signal increased linearly with the square root of the measurement time, with narrow 95 % confidence bands (Figure S17).

S3. Solid-state NMR spectroscopy

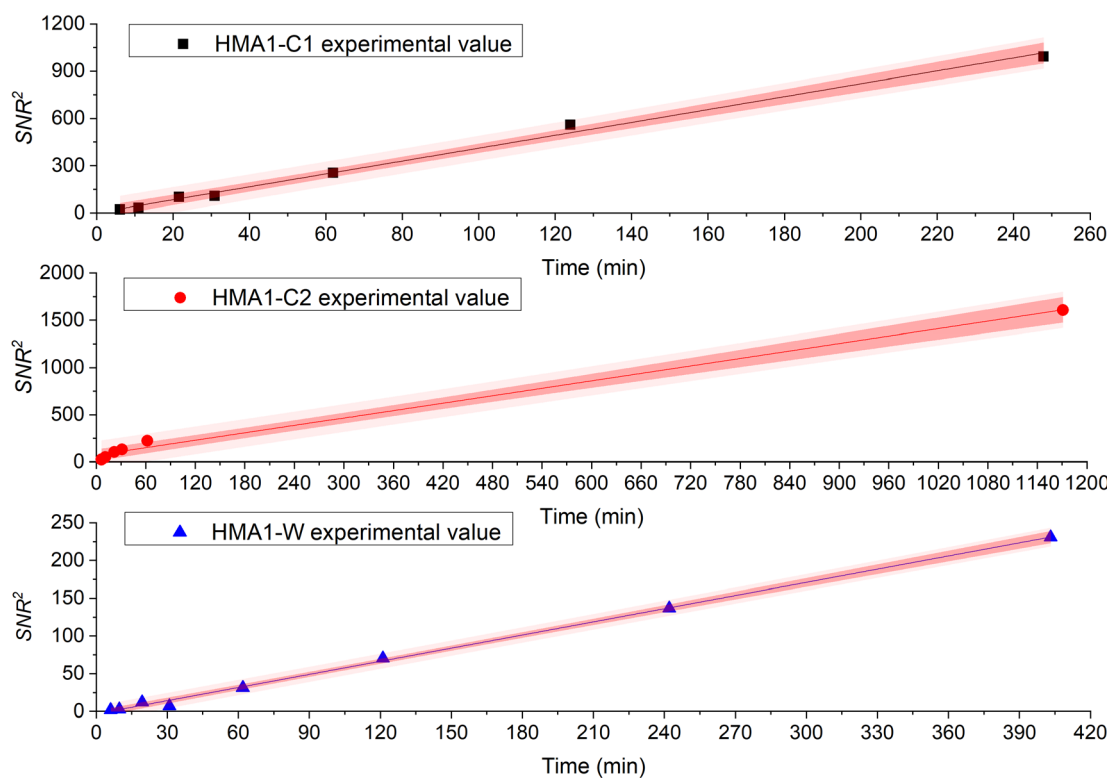


Figure S17: Square of the SNR of ^{13}C NMR signal at 71 ppm for various measurement times for (top) HMA1-C1, (middle) HMA1-C2, and (bottom) HMA1-W with experimental data (symbols), linear fit (solid line) and 95 % confidence bands (dark pink zones).

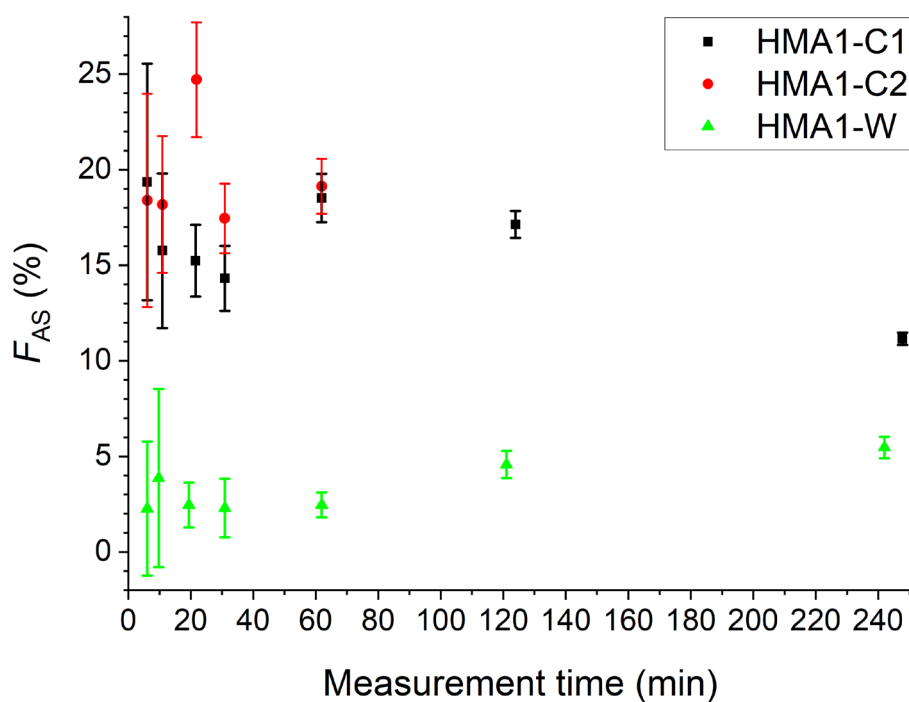


Figure S18: Antistatic1 content (F_{AS}) for HMA1-C1, HMA1-C2, and HMA1-W for different measurement times (error bars represent the standard deviation calculated using Eq. 4).

S3.4. ^1H relaxation NMR

S3.4.1. T_2^* data treatment

^1H NMR spectra of HMA7 were acquired at different temperatures (Figure S19). The apparent transversal relaxation time T_2^* was determined from the line width of the two main signals in ^1H NMR spectra (through the full width at half maximum, using Eq. S3).³⁴ T_2^* increased with increasing temperature which was indicative of an increase in mobility (Figure S20). Due to multiple overlapping signals, the determined T_2^* was representative of multiple components with superimposition and could not resolve the behavior of the individual components. Furthermore, due to the mobility differences in composite materials, ^1H NMR spectra cannot be decomposed into a few components conclusively.

$$T_2^* = \frac{1}{\pi \cdot FWHM}$$

S3

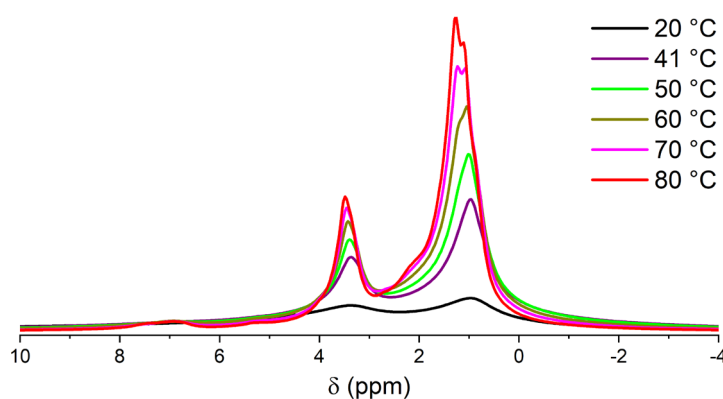


Figure S19: ^1H NMR spectra of HMA7 at different temperatures.

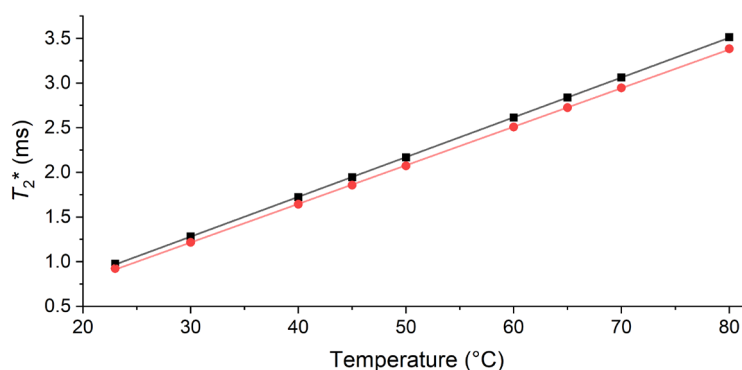


Figure S20: T_2^* of HMA7 determined using Eq. S3 for the signals around 1 ppm (squares) and 3.5 ppm (circles) plotted with linear fits (solid lines, $y=90.72 \cdot (x+1.42)^{-1.87}$ with $R^2=0.92$ and $y=2.95 \cdot (x+11.63)^{16.01}$ with $R^2=0.92$, respectively).

S3.4.2. T_2 relaxation times

T_2 values were determined from the measured decays (such as Figure 21) with the Origin 2016 software (such as Figure S21).

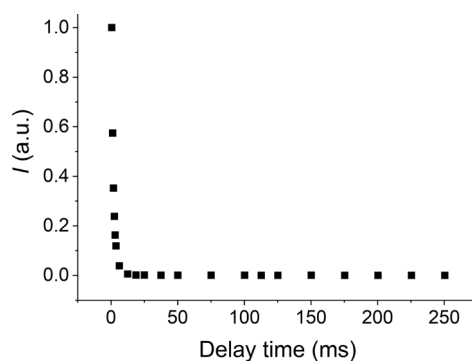


Figure S21: Signal integral vs delay time for HMA7 at 23 °C.

The data was plotted as the natural logarithm of the signal integral vs delay time (Figure S22a) and three linear regions A, B and C identified. It meant that there were three different components within the decay and these could be related to the different parts of the HMA BaseResin1, which is a polyamide made up of diacid and diamine building blocks.

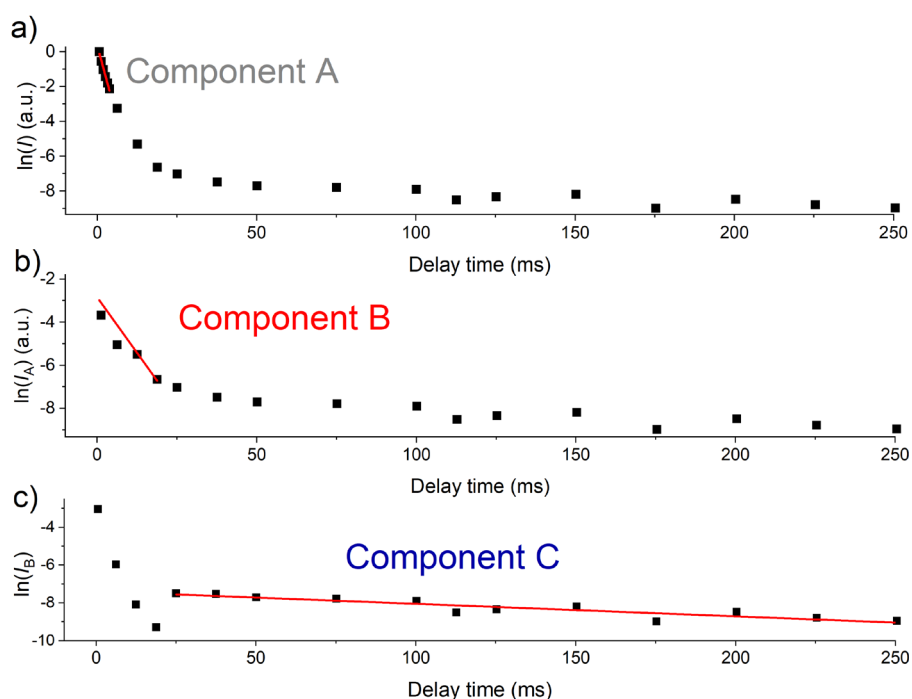


Figure S22: (a) Natural logarithm of the signal integral vs delay time for HMA7 at 23 °C with (a) linear fit for component A, (b) linear fit for component B after subtraction of linear fit of component A and (c) linear fit for component C after subtraction of linear fit of components B.

S3. Solid-state NMR spectroscopy

The linearized data was fitted using a succession of Levenberg-Marquardt linear fits. Through a linear fit of $\ln(I)$, the longitudinal relaxation time $T_{2,A}$ of component A was determined with Eq. S4:

$$\ln I = -\frac{t}{T_{2,A}} + \ln A \quad S4$$

where A is a constant and t is the delay time in ms (Figure S22a). The linear fit data was then converted to exponential form and subtracted from I to generate a new decay I_A (Eq. S5):

$$I_A = I - A \cdot e^{-\frac{t}{T_{2,A}}} \quad S5$$

Through a linear fit of $\ln(I_A)$, the longitudinal relaxation time $T_{2,B}$ of component B was determined with Eq. S6:

$$\ln I_A = -\frac{t}{T_{2,B}} + \ln B \quad S6$$

where B is a constant (Figure S22b). The linear fit data was then converted to exponential form and subtracted from I_A to generate a newer decay I_B (Eq. S7):

$$I_B = I_A - B \cdot e^{-\frac{t}{T_{2,B}}} \quad S7$$

Through a linear fit of $\ln(I_B)$, the longitudinal relaxation time $T_{2,C}$ of component C was determined with Eq. S8:

$$\ln I_B = -\frac{t}{T_{2,C}} + \ln C \quad S8$$

where C is a constant (Figure S22c). The determined $T_{2,A}$, $T_{2,B}$ and $T_{2,C}$ values at different temperature, and at different F_{AS} along with their errors are listed in Table S5 and Table S7. The linear fits used to determine $T_{2,A}$, $T_{2,B}$ and $T_{2,C}$ for HMA7 at different temperatures, and $T_{2,A}$, $T_{2,B}$ and $T_{2,C}$ at different F_{AS} all had high coefficients of determination, excluding two fits (Table S6 and Table S8).

Table S5: $T_{2,A}$, $T_{2,B}$, and $T_{2,C}$ along with error values for HMA7 at different temperatures T .

T (°C)	$T_{2,A}$ (ms)	$T_{2,A}^{\text{error}}$ (ms)	$T_{2,B}$ (ms)	$T_{2,B}^{\text{error}}$ (ms)	$T_{2,C}$ (ms)	$T_{2,C}^{\text{error}}$ (ms)
23.6	1.76	0.08	5.34	0.21	169.5	27.8
37.3	1.97	0.15	8.68	2.07	213.2	100.9
45.7	2.55	0.17	12.52	1.13	233.1	154.9
55.2	2.96	0.21	14.96	1.47	73.7	31.4
65.7	3.52	0.23	23.21	2.07	56.9	21.0
75.2	4.26	0.21	32.37	3.18	62.7	11.5

S3. Solid-state NMR spectroscopy

85.7	5.25	0.19	47.30	2.33	71.7	19.5
------	------	------	-------	------	------	------

Table S6: Coefficient of determination R^2 of the linear fits used to determine $T_{2,A}$, $T_{2,B}$ and $T_{2,C}$ for HMA7 at different temperatures T .

T (°C)	R^2		
	$T_{2,A}$	$T_{2,B}$	$T_{2,C}$
23.6	0.98	0.76	0.76
37.3	0.98	0.73	0.23
45.7	0.98	0.96	0.12
55.2	0.98	0.96	0.43
65.7	0.98	0.96	0.47
75.2	0.99	0.97	0.80
85.7	0.99	0.98	0.71

Table S7: $T_{2,A}$, $T_{2,B}$ and $T_{2,C}$ along with error values at different F_{AS} at room temperature.

F_{AS} (%)	$T_{2,A}$ (ms)	$T_{2,A}^{\text{error}}$ (ms)	$T_{2,B}$ (ms)	$T_{2,B}^{\text{error}}$ (ms)	$T_{2,C}$ (ms)	$T_{2,C}^{\text{error}}$ (ms)
5.6	1.81	0.10	12.89	0.80	31.15	4.68
11.2	1.97	0.13	13.17	0.25	34.59	13.36
15.7	1.94	0.11	13.30	0.41	37.59	5.26
21.6	2.10	0.13	14.49	0.37	92.00	22.60

Table S8: Coefficient of determination R^2 of the linear fits used to determine $T_{2,A}$, $T_{2,B}$ and $T_{2,C}$ at different F_{AS} .

F_{AS} (%)	R^2		
	$T_{2,A}$	$T_{2,B}$	$T_{2,C}$
5.6	0.98	0.98	0.86
11.2	0.98	0.99	0.53
15.7	0.98	0.99	0.87
21.6	0.98	0.99	0.66

S3.4.3. T_2 pre-exponential factors

The pre-exponential factors of the three decays, A_A , A_B , and A_C (defined as $1 - A_A - A_B$), were determined through a fit with a tri-exponential decay function (Eq. S9), for which the T_2 values were set to values determined above (Table S5 and Table S7).

$$I = A_A e^{-\frac{t}{T_{2,A}}} + A_B e^{-\frac{t}{T_{2,B}}} + (1 - A_A - A_B) e^{-\frac{t}{T_{2,C}}} \quad \text{S9}$$

S3. Solid-state NMR spectroscopy

The pre-exponential factor of each component of the CPMG decay was determined at different temperatures (Figure S9) and F_{AS} (Figure S10) to investigate the contributions of the three decays to the total signal.

Table S9: Pre-exponential factors for the tri-exponential decay function defining the T_2 decay for HMA7 at different temperatures T .

T (°C)	A_A (%)	A_A^{error} (%)	A_B (%)	A_B^{error} (%)	$1-A_A-A_B$ (%)
23.6	88.2	8.5	12.6	10.2	-0.9
37.3	79.2	5.3	21.9	6.7	14.1
45.7	84.7	4.2	16.0	5.4	-0.7
55.2	78.0	3.9	24.0	6.7	-2.0
65.7	77.7	3.2	25.2	8.3	-2.8
75.2	78.8	2.7	26.4	8.9	-5.3
85.7	73.8	2.2	29.7	10.4	-3.5

Table S10: Pre-exponential factors for the tri-exponential decay function defining the T_2 decay at different F_{AS} at room temperature.

F_{AS} (%)	A_A (%)	A_A^{error} (%)	A_B (%)	A_B^{error} (%)	$1-A_A-A_B$ (%)
5.6	80	5	30	15	10
11.2	80	5	27	12	7
15.7	80	5	27	12	7
21.6	81	4	21	7	2

S3.5. 2D-WISE NMR

S3.5.1. Optimization

The parameters for the acquisition of 2D-WISE spectra needed to be optimized to have enough resolution in ^1H dimension (see Figures S23-S24 and S26 for 100, 80, and 40 increments) in a reasonable measuring time (see Figures S23-S26 for 30, 20, 10, and 5 μs between increments, and Figures S26-29 for 832, 1576, 2048 and 4776 scans). A compromise was found to observe most signals with repeatable FWHM of the extracted 1D ^1H NMR spectra (see Figures S30-34) at different ^{13}C resonances (Figure S35) and sufficient SNRs (Figure S36) with 40 increments of 5 μs for the acquisition in the indirect ^1H dimension, and about 5,000 scans.

S3.5.1.1. 2D-WISE NMR spectra

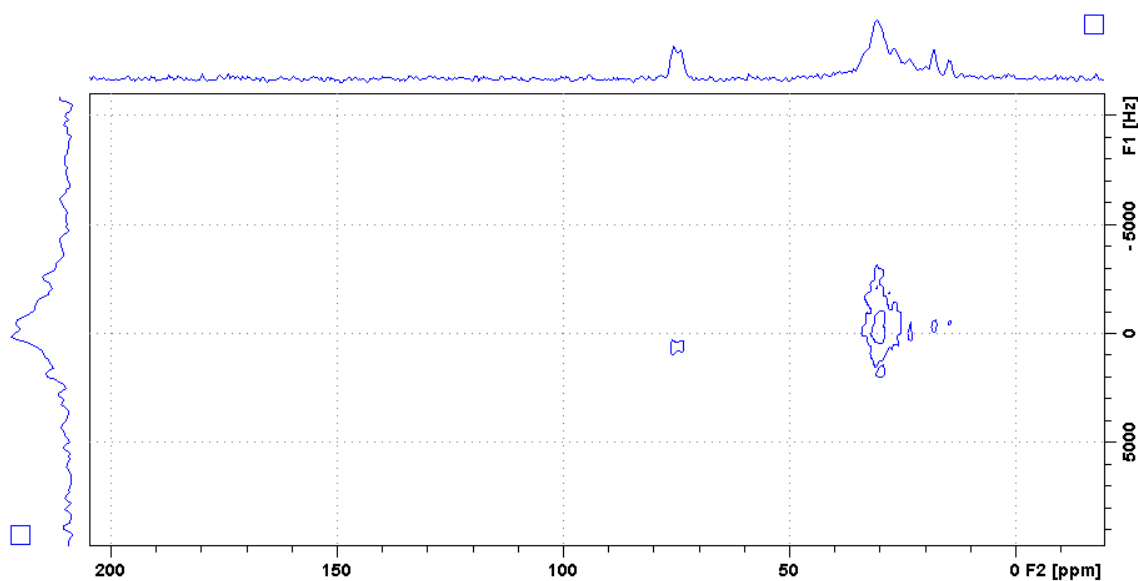


Figure S23: 2D-WISE spectrum for HMA7 (no 180° pulse, 100 increments of $30 \mu\text{s}$ for the acquisition in the indirect ^1H dimension, 352 scans in direct ^{13}C dimension, see Table S3 for ^{13}C NMR signal assignment).

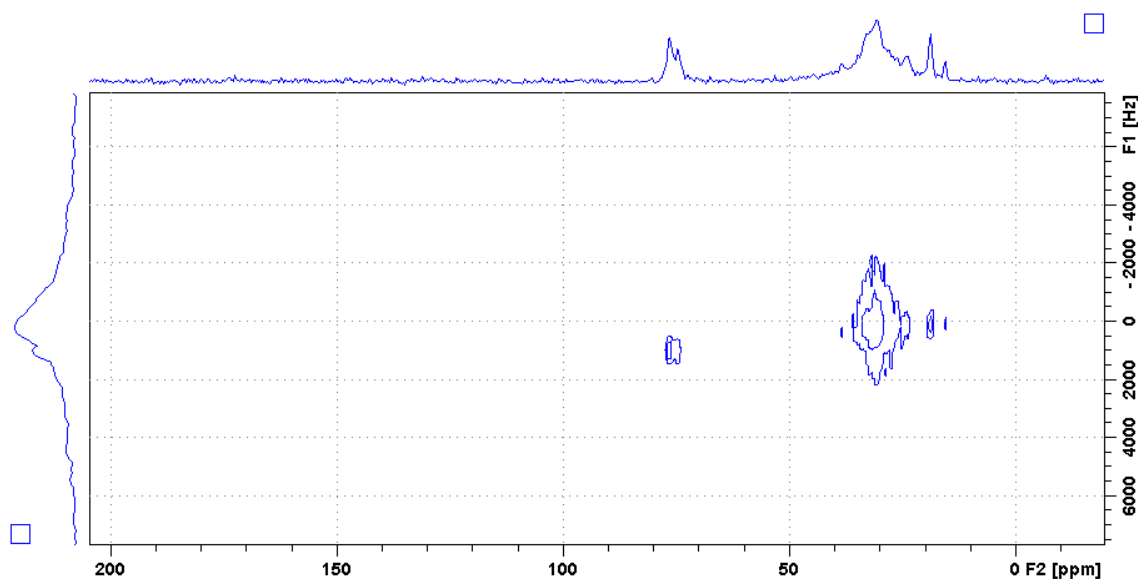


Figure S24: 2D-WISE spectrum for HMA7 (no 180° pulse, 80 increments of $20 \mu\text{s}$ for the acquisition in the indirect ^1H dimension, 1280 scans in direct ^{13}C dimension, see Table S3 for ^{13}C NMR signal assignment).

S3. Solid-state NMR spectroscopy

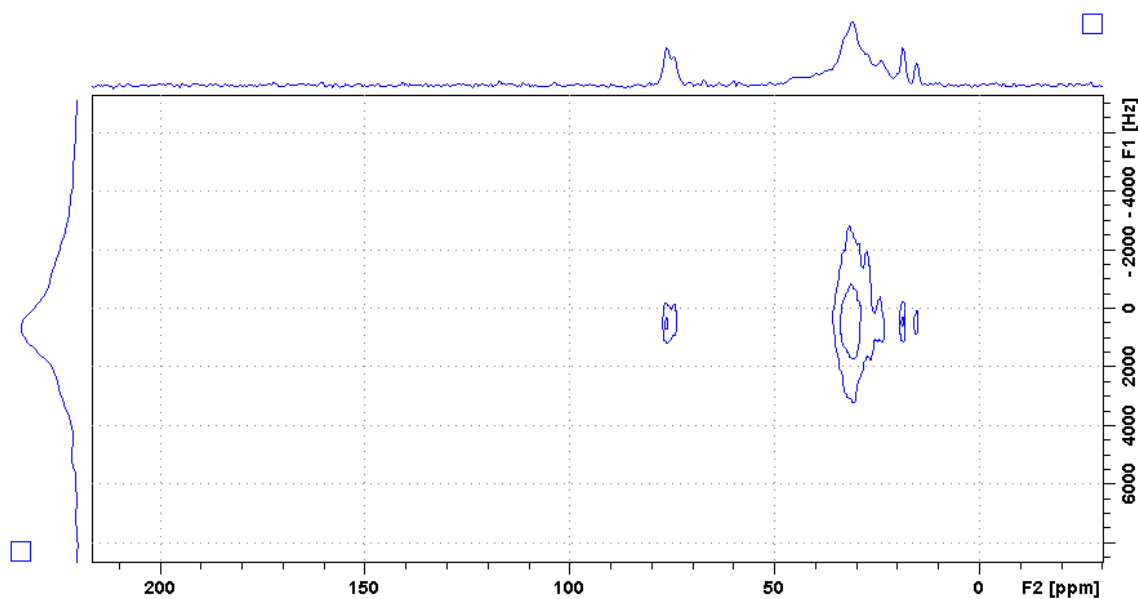


Figure S25: 2D-WISE spectrum for HMA7 (80 increments of 10 μ s for the acquisition in the indirect ^1H dimension, 1280 scans in direct ^{13}C dimension, see Table S3 for ^{13}C NMR signal assignment).

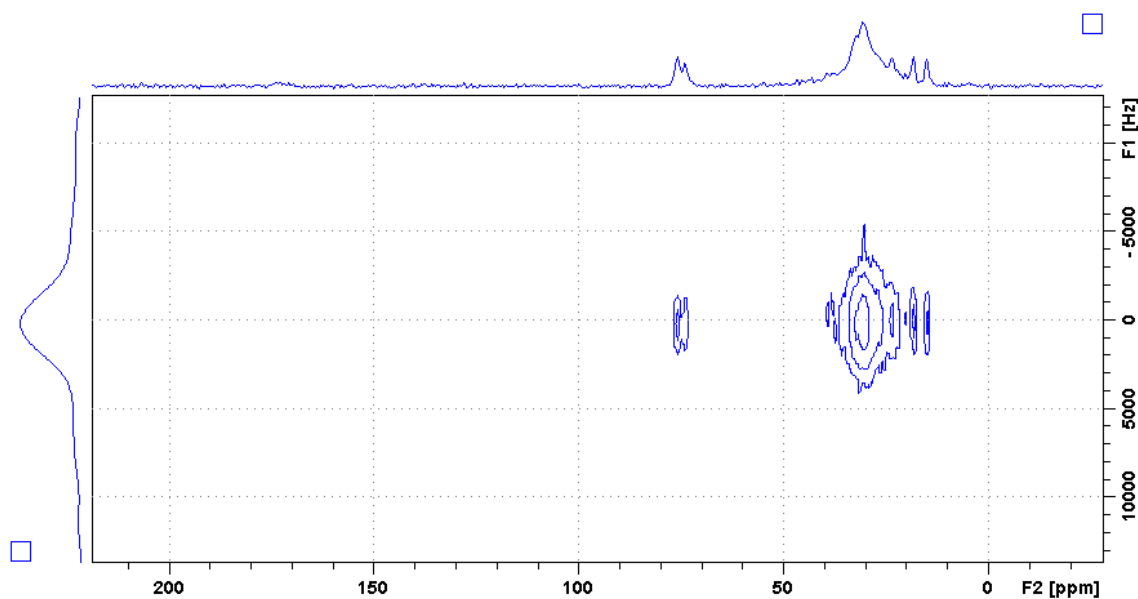


Figure S26: 2D-WISE spectrum for HMA7 (40 increments of 5 μ s for the acquisition in the indirect ^1H dimension, 832 scans in direct ^{13}C dimension, see Table S3 for ^{13}C NMR signal assignment).

S3. Solid-state NMR spectroscopy

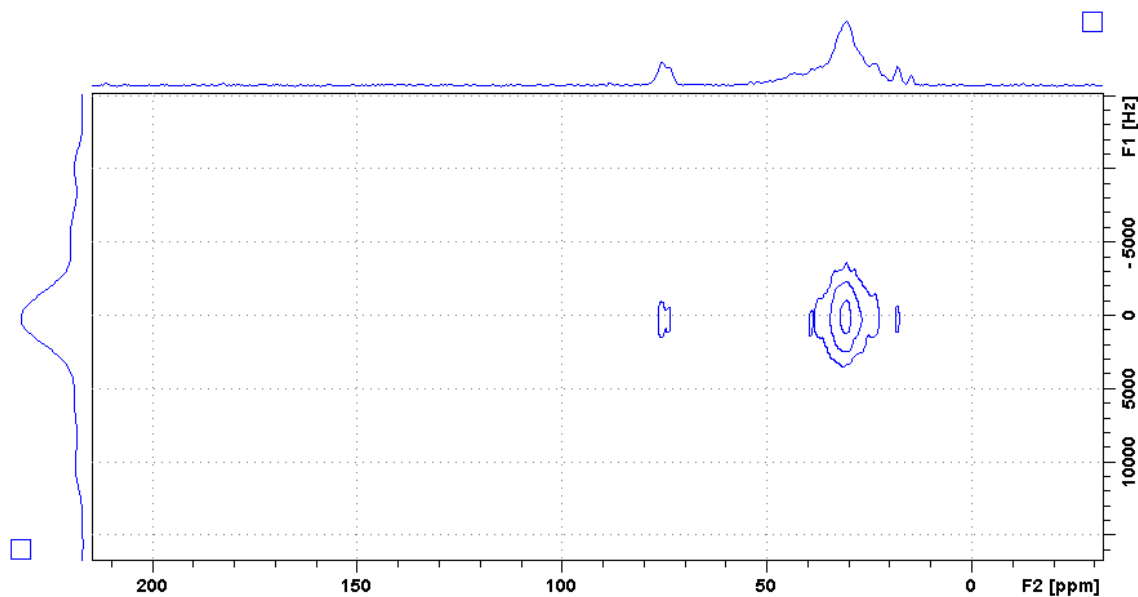


Figure S27: 2D-WISE spectrum for HMA7 (40 increments of 5 μs for the acquisition in the indirect ^1H dimension, 1576 scans in direct ^{13}C dimension, see Table S3 for ^{13}C NMR signal assignment).

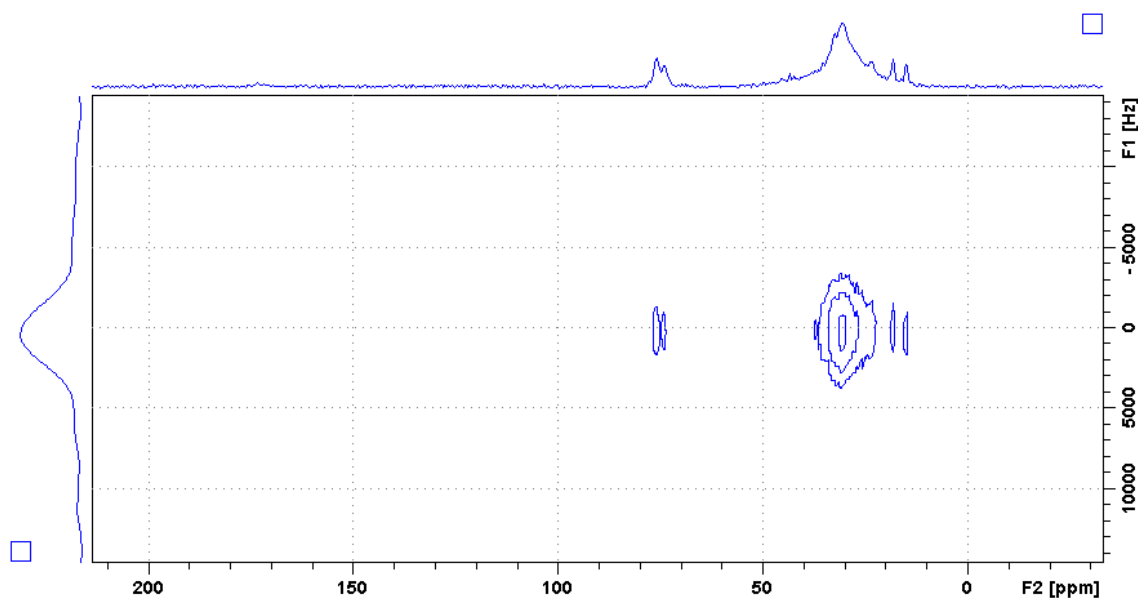


Figure S28: 2D-WISE spectrum for HMA7 (40 increments of 5 μs for the acquisition in the indirect ^1H dimension, 2048 scans in direct ^{13}C dimension, see Table S3 for ^{13}C NMR signal assignment).

S3. Solid-state NMR spectroscopy

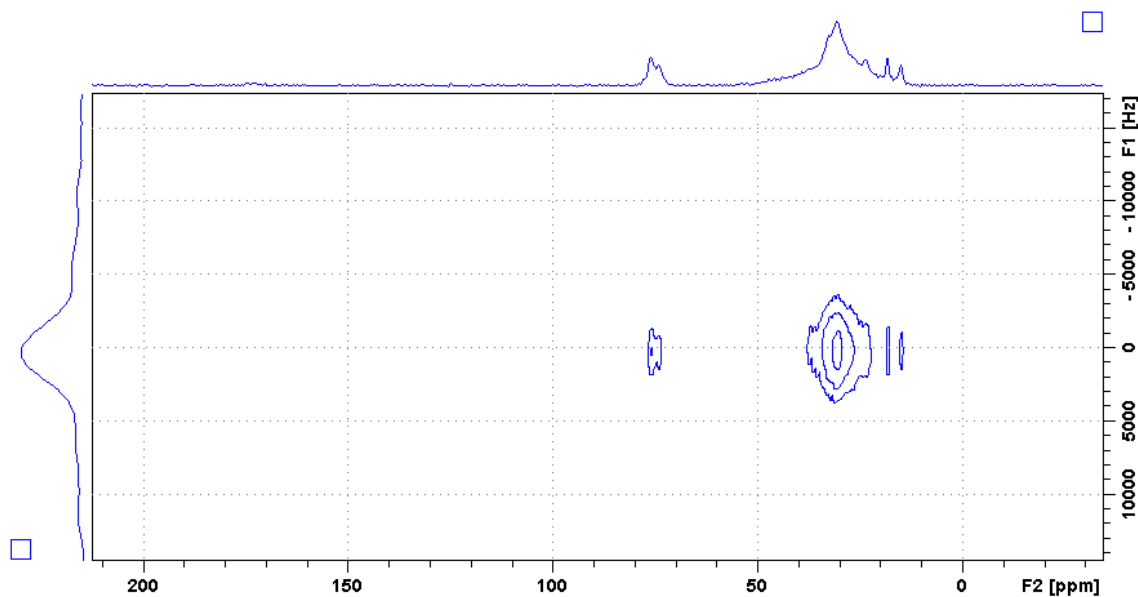


Figure S29: 2D-WISE spectrum for HMA7 (40 increments of 5 μs for the acquisition in the indirect ^1H dimension, 4776 scans in direct ^{13}C dimension, see Table S3 for ^{13}C NMR signal assignment).

S3.5.1.2. 1D ^1H NMR spectra

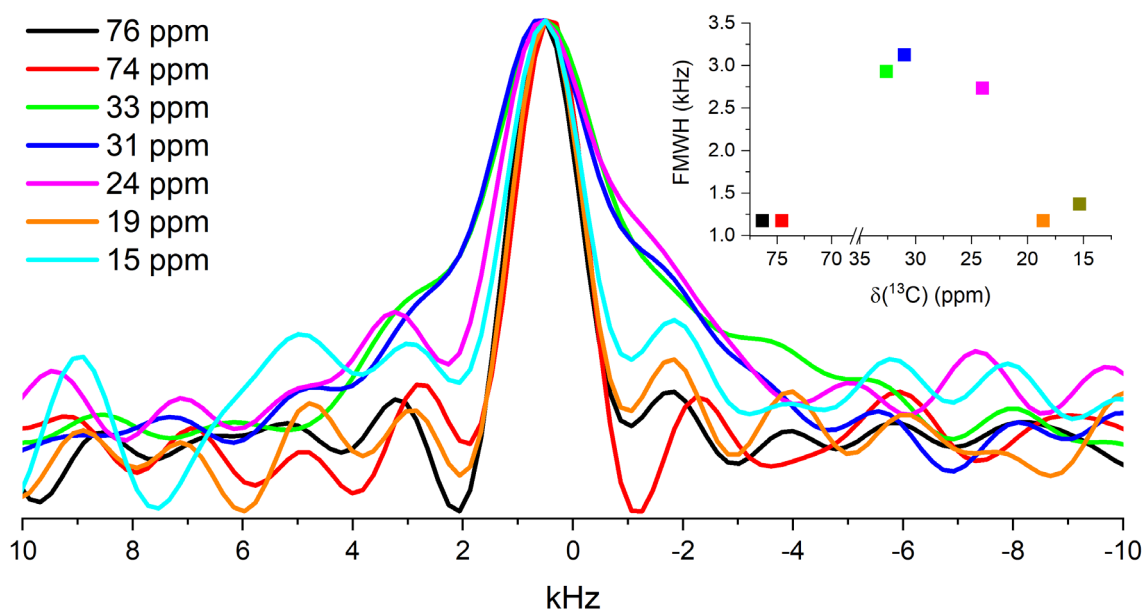


Figure S30: 1D ^1H NMR spectra extracted from 2D-WISE spectrum of HMA7 shown in Figure S25 (normalized to the same maximal signal intensity). The corresponding ^{13}C chemical shifts (see Table S3 for signal assignment) are listed in the graph key and plotted against the corresponding ^1H FWHM (inset).

S3. Solid-state NMR spectroscopy

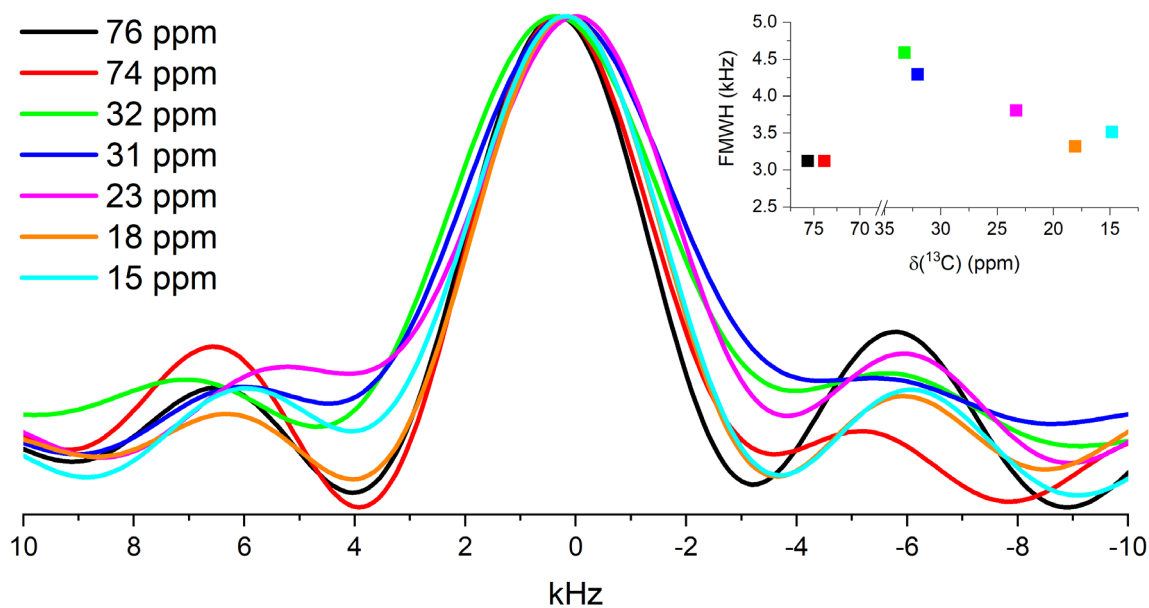


Figure S31: $1\text{D } ^1\text{H}$ NMR spectra extracted from 2D-WISE spectrum of HMA7 shown in Figure S26 (normalized to the same maximal signal intensity). The corresponding ^{13}C chemical shifts (see Table S3 for signal assignment) are listed in the graph key and plotted against their full width at half maximum (FWHM, inset).

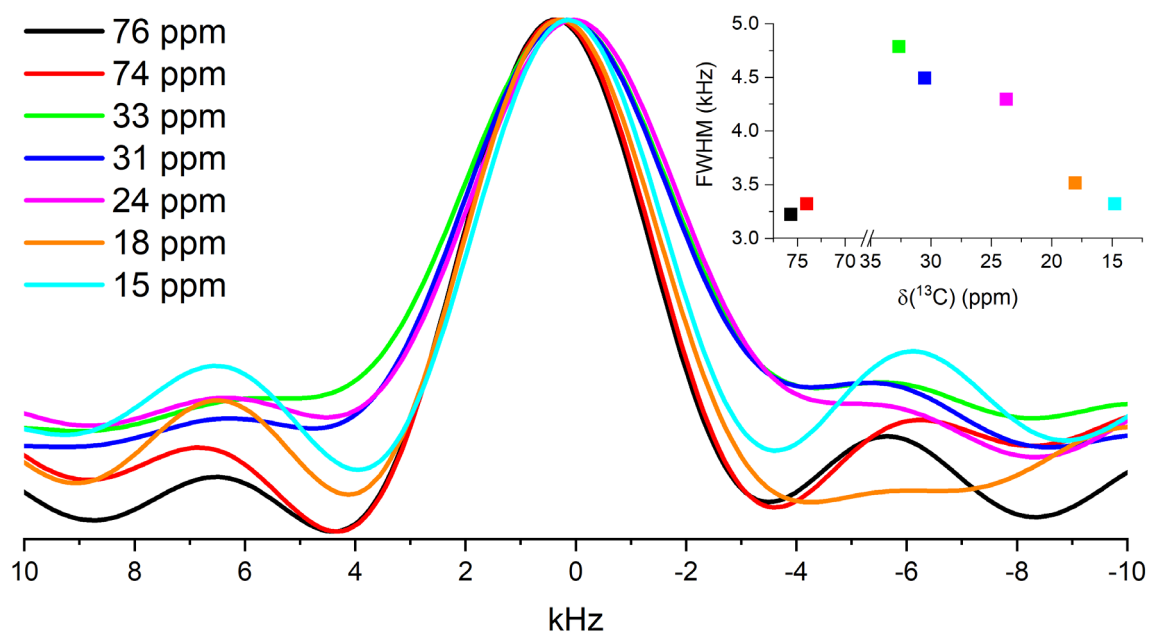


Figure S32: $1\text{D } ^1\text{H}$ NMR spectra extracted from 2D-WISE spectrum of HMA7 shown in Figure S27 (normalized to the same maximal signal intensity). The corresponding ^{13}C chemical shifts (see Table S3 for signal assignment) are listed in the graph key and plotted against their full width at half maximum (FWHM, inset).

S3. Solid-state NMR spectroscopy

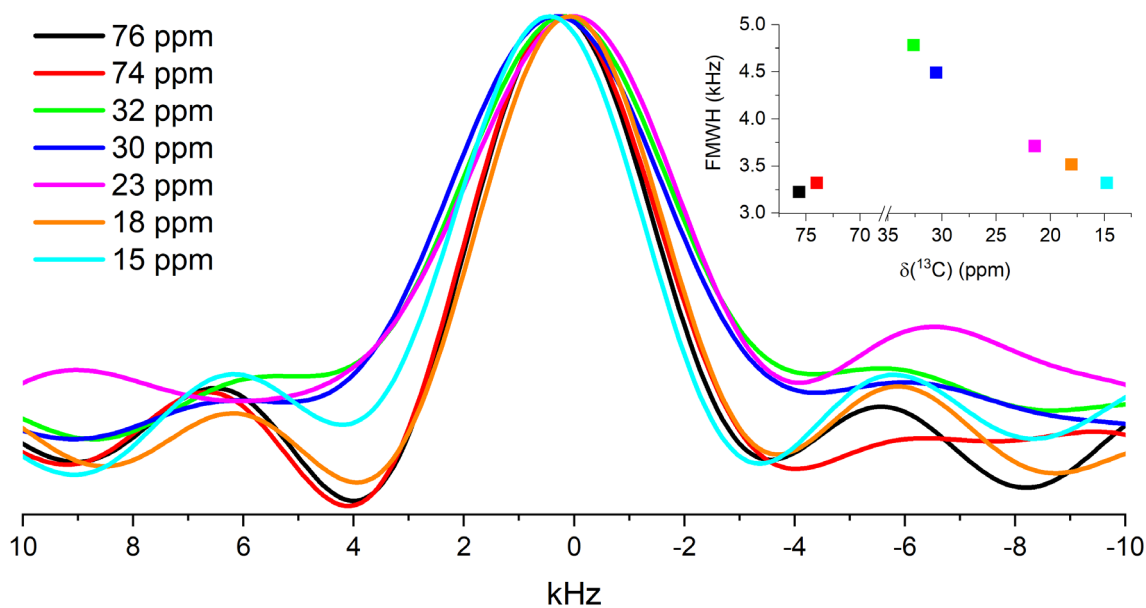


Figure S33: $1\text{D } ^1\text{H}$ NMR spectra extracted from 2D-WISE spectrum of HMA7 shown in Figure S28 (normalized to the same maximal signal intensity). The corresponding ^{13}C chemical shifts (see Table S3 for signal assignment) are listed in the graph key and plotted against their full width at half maximum (FWHM, inset).

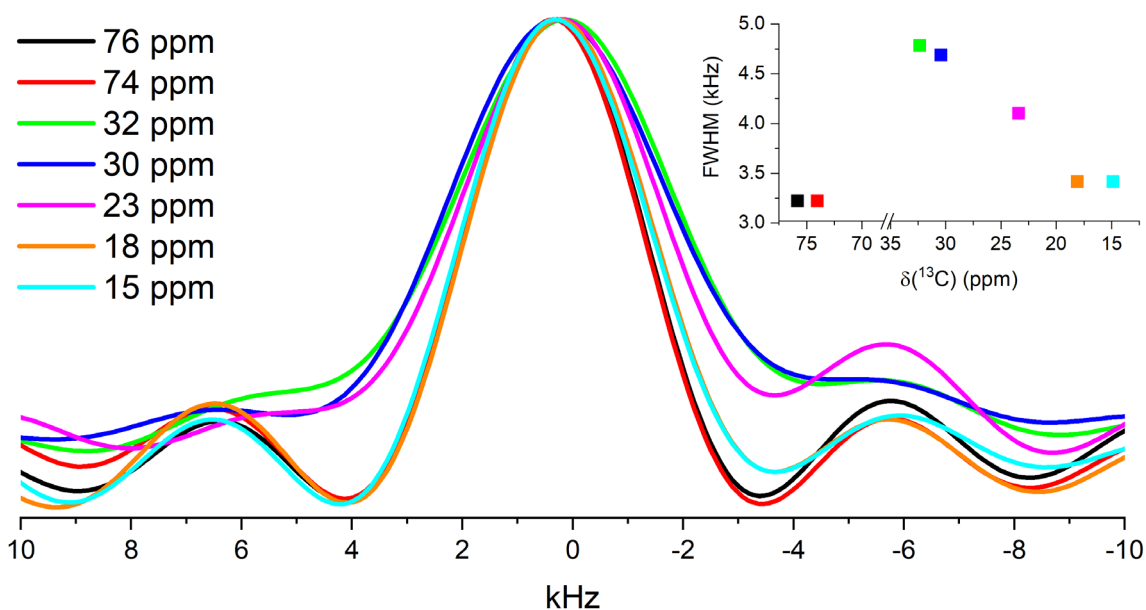


Figure S34: $1\text{D } ^1\text{H}$ NMR spectra extracted from 2D-WISE spectrum of HMA7 shown in Figure S29 (normalized to the same maximal signal intensity). The corresponding ^{13}C chemical shifts (see Table S3 for signal assignment) are listed in the graph key and plotted against their full width at half maximum (FWHM, inset).

S3. Solid-state NMR spectroscopy

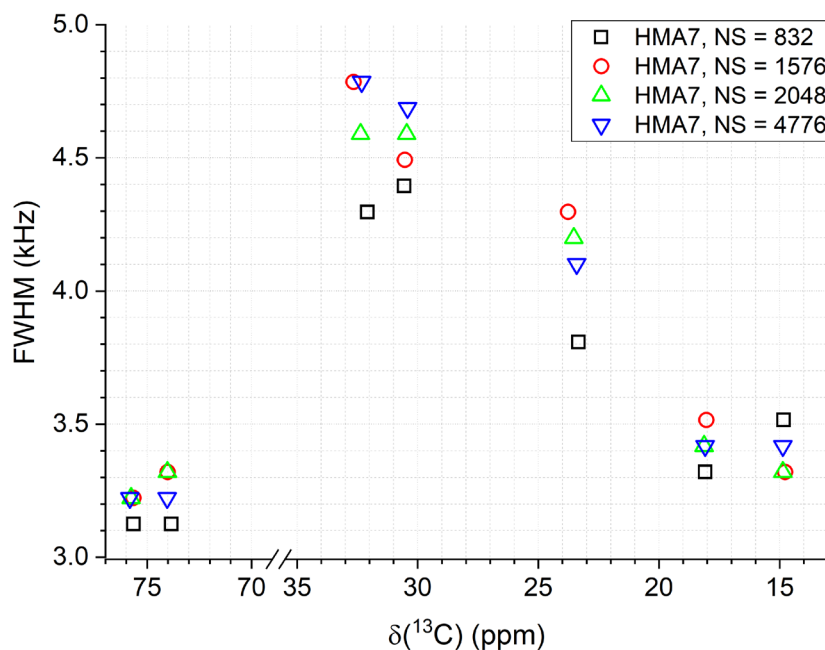


Figure S35: FWHM of 1D ^1H NMR spectra extracted from 2D-WISE spectra of HMA7 with different number of scans (832, 1576, 2048, and 4776) shown in Figures S26-S27 at various ^{13}C resonances (see Table S3 for ^{13}C NMR signal assignment).

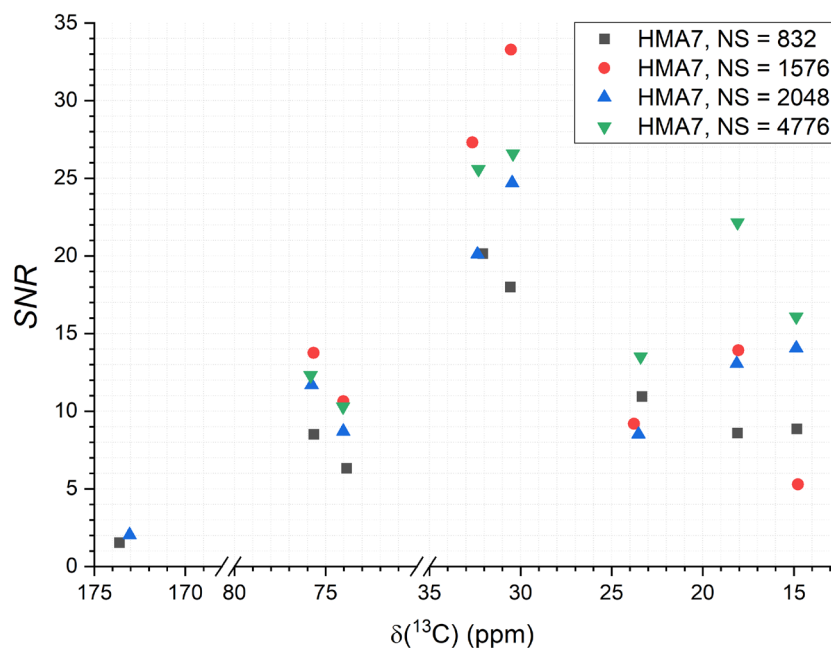


Figure S36: SNR of the 1D ^1H NMR spectra extracted from 2D-WISE spectra of HMA7 with different number of scans (832, 1576, 2048 and 4776) shown in Figures S26-S27 at various ^{13}C resonances (see Table S3 for ^{13}C NMR signal assignment).

S3.5.2. Measurements

S3.5.2.1. 2D-WISE NMR spectra

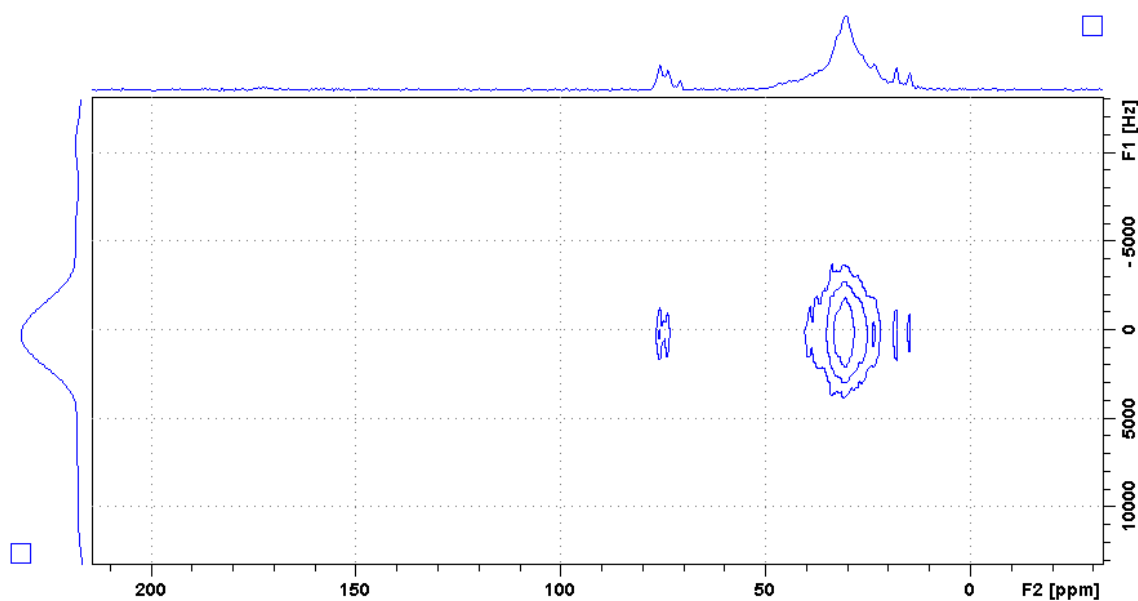


Figure S37: 2D-WISE spectrum for HMA1 (40 increments of 5 μs for the acquisition in the indirect ^1H dimension, 5240 scans in direct ^{13}C dimension, see Table S3 for ^{13}C NMR signal assignment).

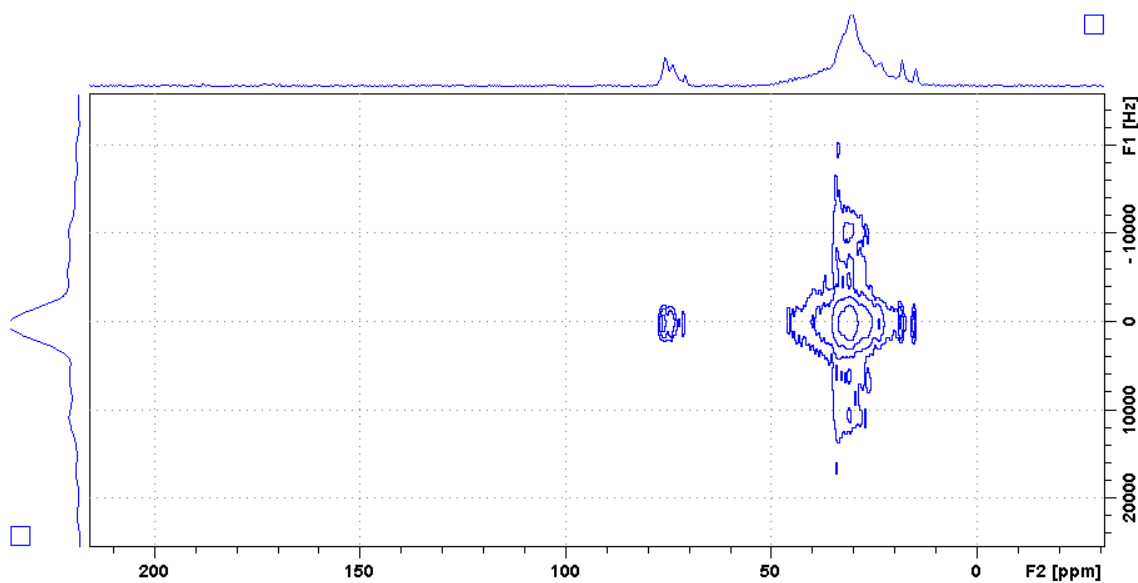


Figure S38: 2D-WISE spectrum for HMA1-C1 (40 increments of 5 μs for the acquisition in the indirect ^1H dimension, 5144 scans in direct ^{13}C dimension, see Table S3 for ^{13}C NMR signal assignment).

S3. Solid-state NMR spectroscopy

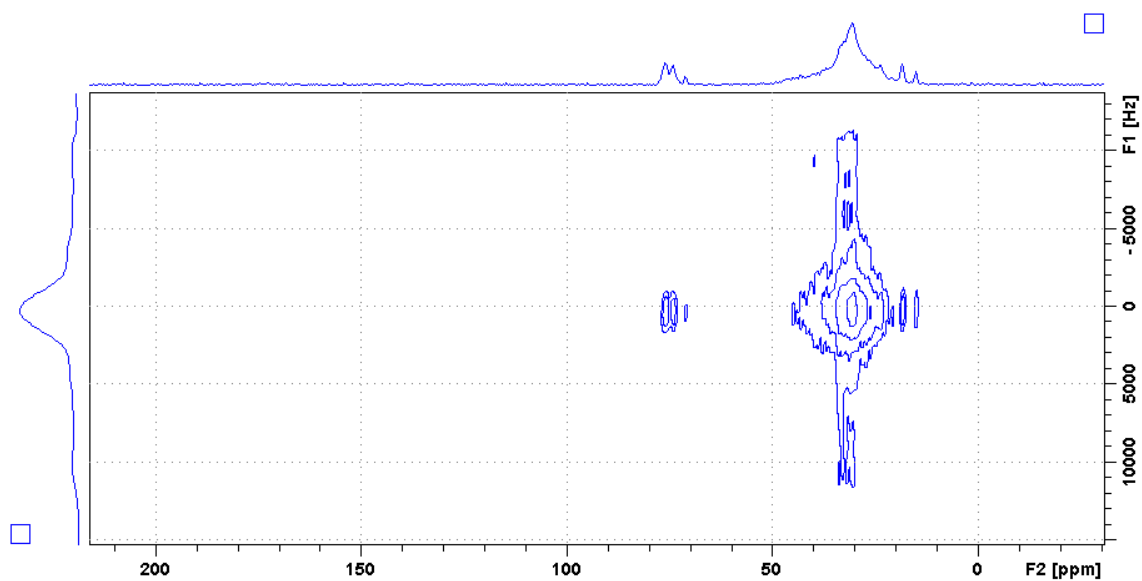


Figure S39: 2D-WISE spectrum for HMA1-C2 (40 increments of 5 μ s for the acquisition in the indirect 1 H dimension, 4776 scans in direct 13 C dimension, see Table S3 for 13 C NMR signal assignment).

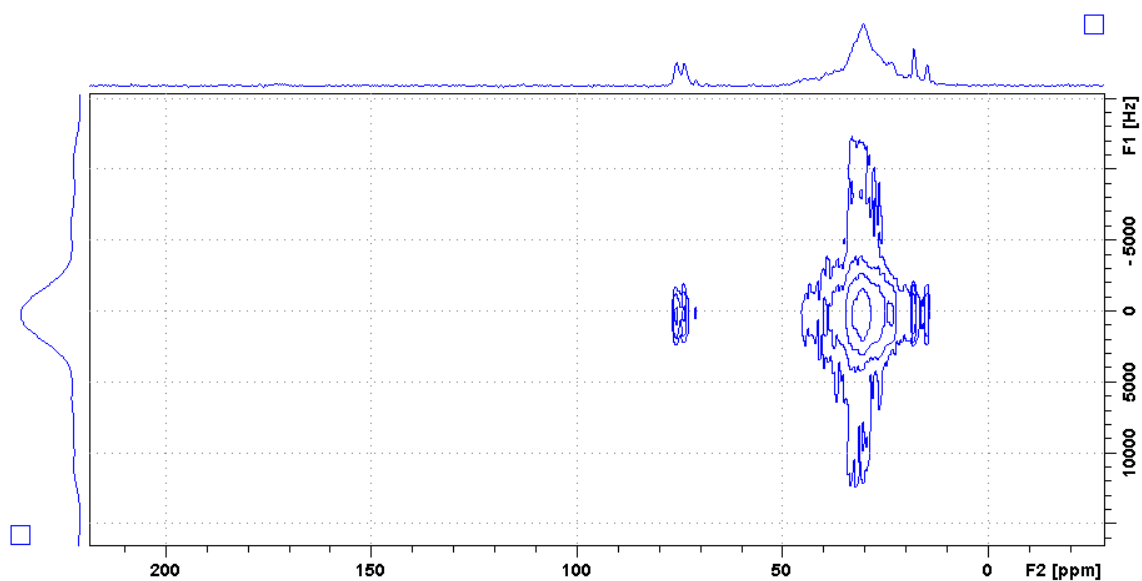


Figure S40: 2D-WISE spectrum for HMA1-W (40 increments of 5 μ s for the acquisition in the indirect 1 H dimension, 5144 scans in direct 13 C dimension, see Table S3 for 13 C NMR signal assignment).

S3. Solid-state NMR spectroscopy

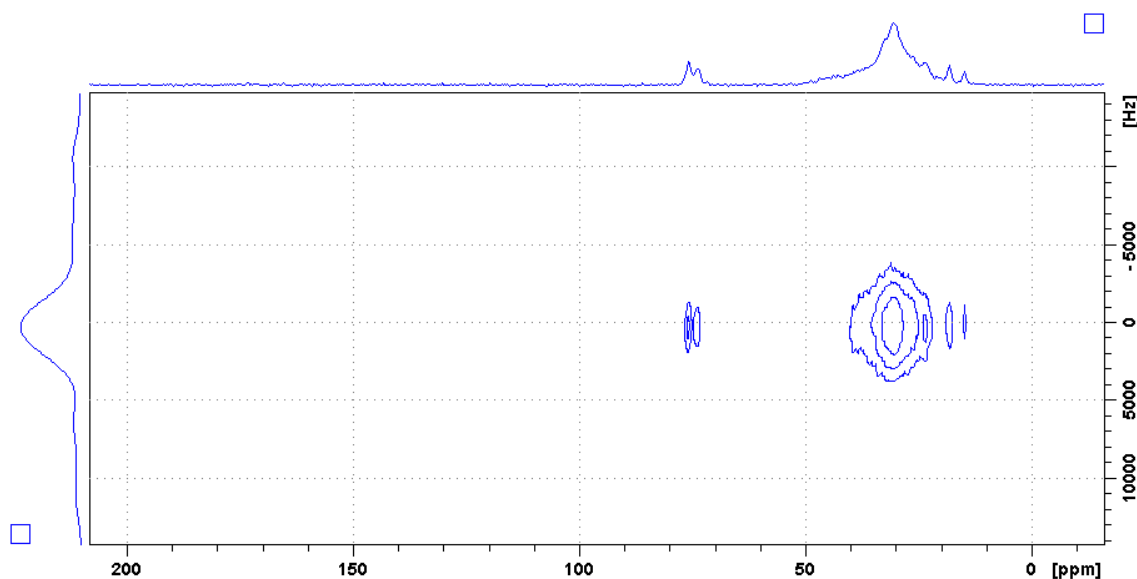


Figure S41: 2D-WISE spectrum for BaseResin1 (40 increments of 5 μ s for the acquisition in the indirect ^1H dimension, 4856 scans in direct ^{13}C dimension, see Table S3 for ^{13}C NMR signal assignment).

S3.5.2.2. 1D ^1H NMR spectra

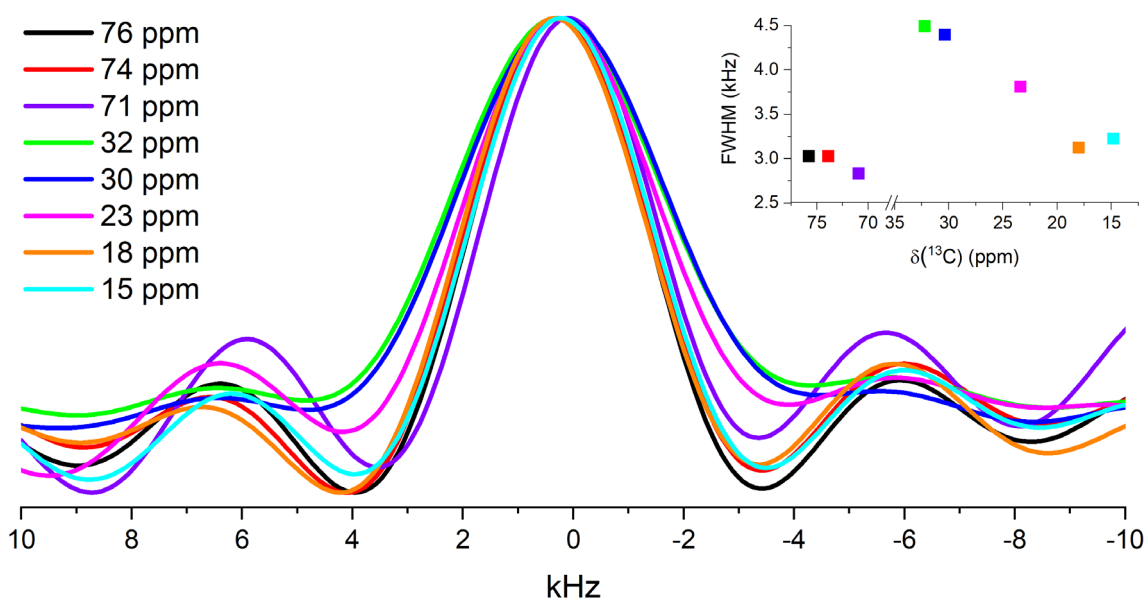


Figure S42: 1D ^1H NMR spectra extracted from 2D-WISE spectrum of HMA1 shown in Figure S37 (normalized to the same maximal signal intensity). The corresponding ^{13}C chemical shifts (see Table S3 for signal assignment) are listed in the graph key and plotted against their full width at half maximum (FWHM, inset).

S3. Solid-state NMR spectroscopy

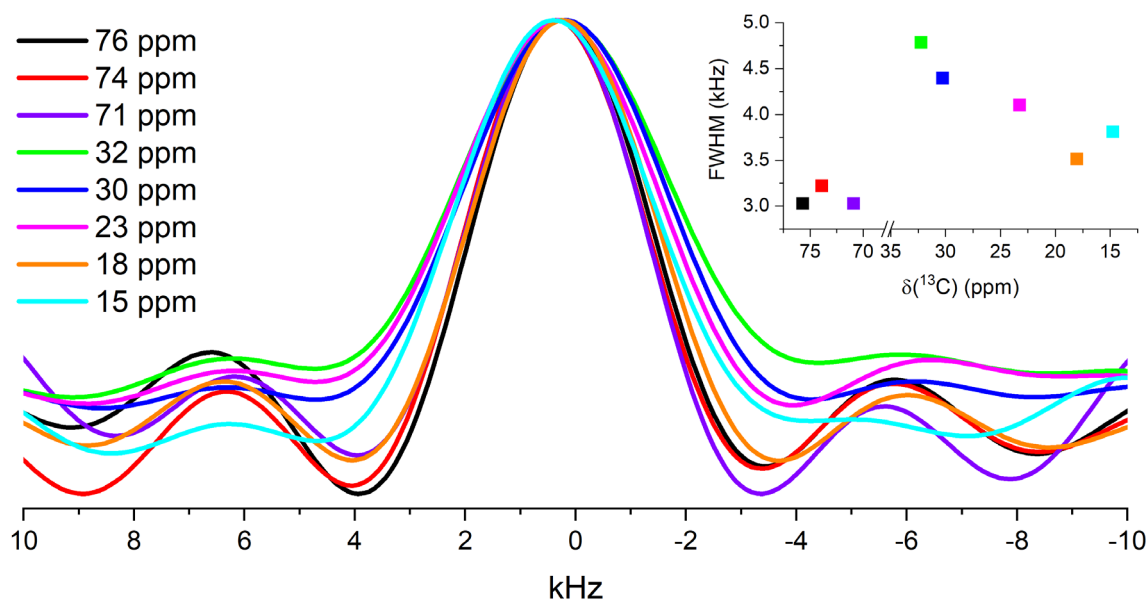


Figure S43: $1D\ ^1H$ NMR spectra extracted from 2D-WISE spectrum of HMA1-C1 shown in Figure S38 (normalized to the same maximal signal intensity). The corresponding ^{13}C chemical shifts (see Table S3 for signal assignment) are listed in the graph key and plotted against their full width at half maximum (FWHM, inset).

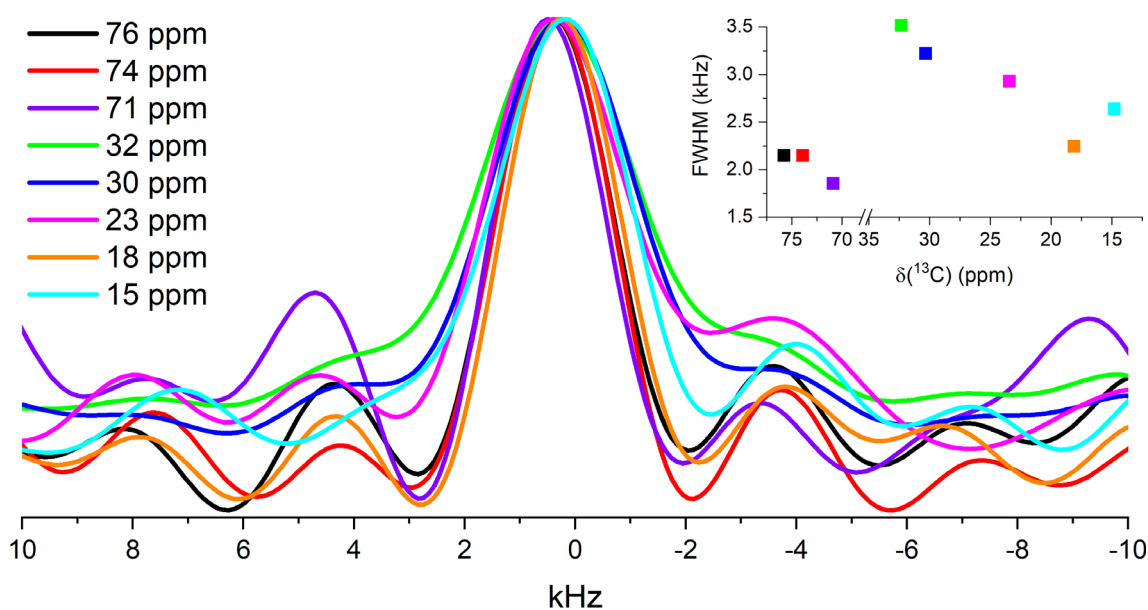


Figure S44: $1D\ ^1H$ NMR spectra extracted from 2D-WISE spectrum of HMA1-C2 shown in Figure S39 (normalized to the same maximal signal intensity). The corresponding ^{13}C chemical shifts (see Table S3 for signal assignment) are listed in the graph key and plotted against their full width at half maximum (FWHM, inset).

S3. Solid-state NMR spectroscopy

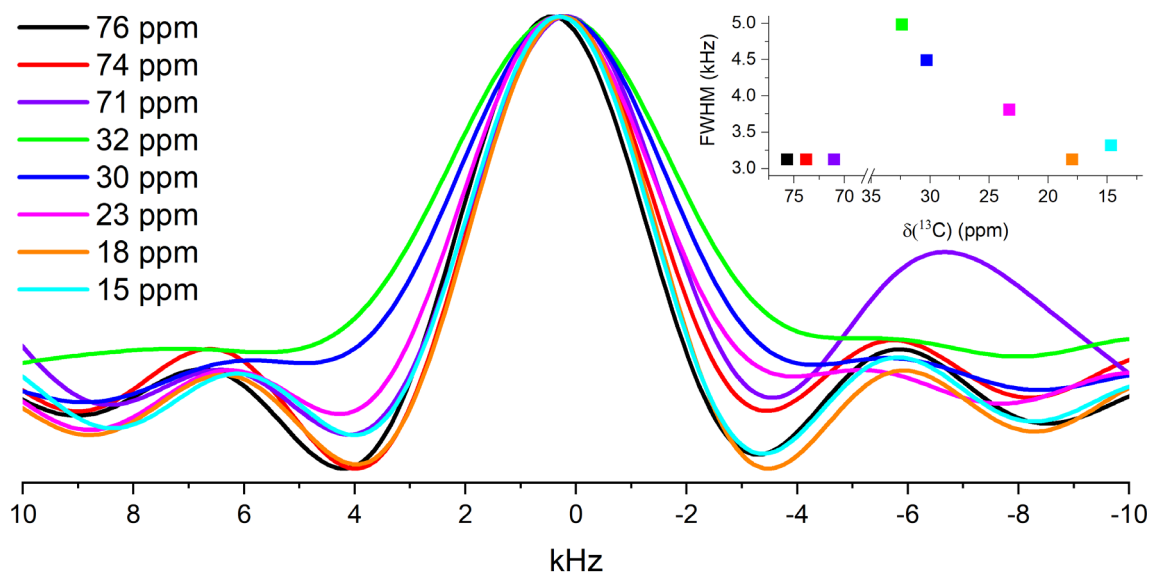


Figure S45: $1D\ ^1H$ NMR spectra extracted from 2D-WISE spectrum of HMA1-W shown in Figure S40 (normalized to the same maximal signal intensity). The corresponding ^{13}C chemical shifts (see Table S3 for signal assignment) are listed in the graph key and plotted against their full width at half maximum (FWHM, inset).

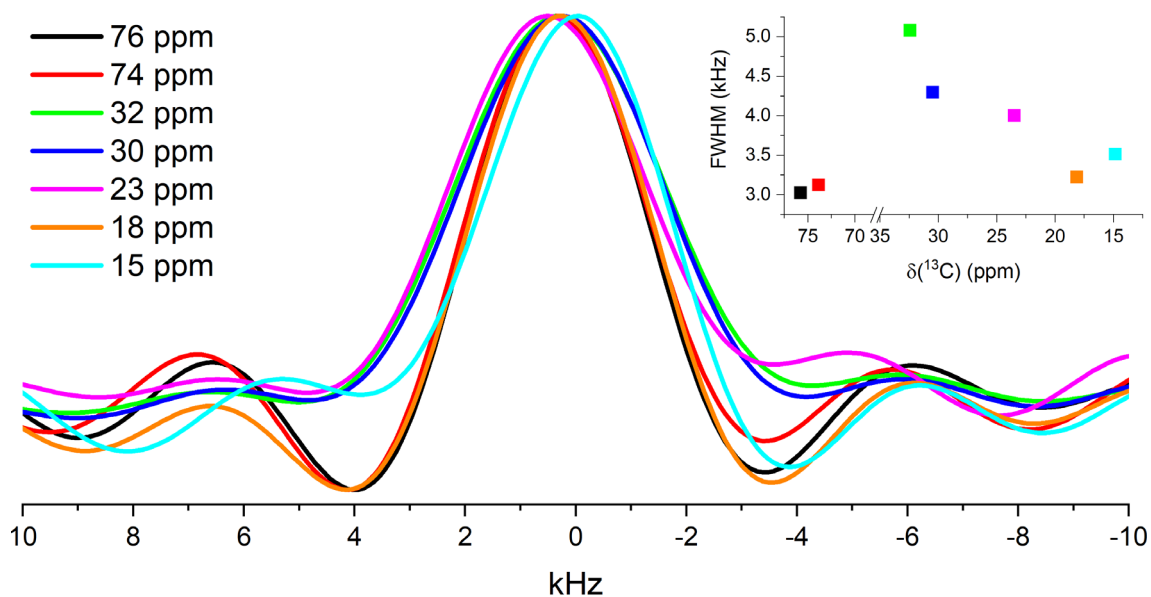


Figure S46: $1D\ ^1H$ NMR spectra extracted from 2D-WISE spectrum of BaseResin1 shown in Figure S41 (normalized to the same maximal signal intensity). The corresponding ^{13}C chemical shifts (see Table S3 for signal assignment) are listed in the graph key and plotted against their full width at half maximum (FWHM, inset).

S4. Scanning electron microscopy

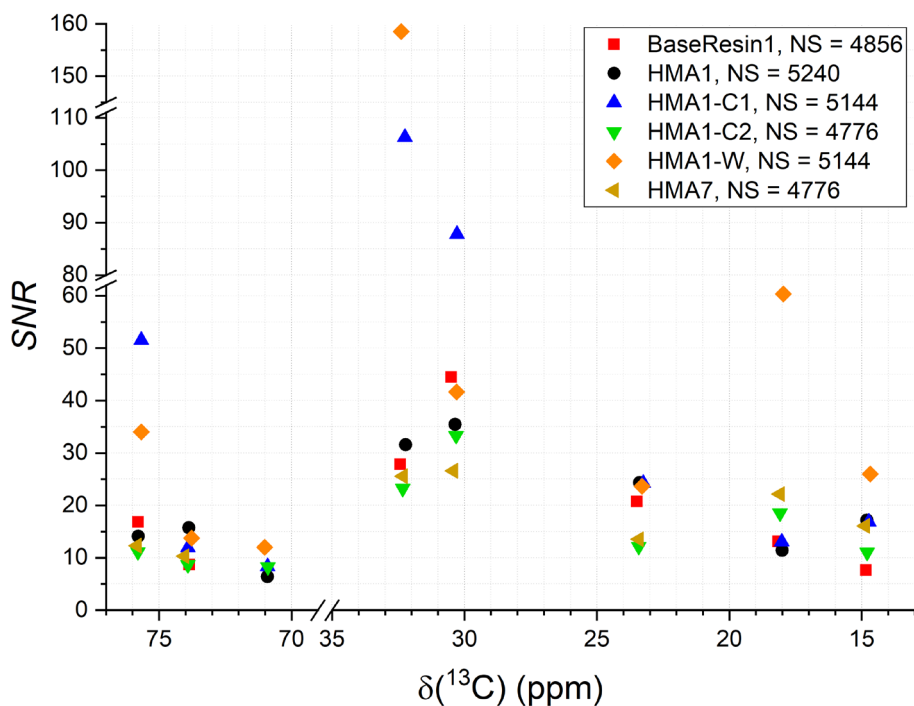


Figure S47: SNR of the 1D ^1H NMR spectra extracted from 2D-WISE spectra of HMA7, HMA1-C2, HMA1-W, HMA1-C1, and BaseResin1 at various ^{13}C resonances (see Table S3 for ^{13}C NMR signal assignment).

S4. Scanning electron microscopy

Scanning electron microscopy (SEM) images of Antistatic1, and BaseResin1 were used to visualize the morphology of the additives before the formulation of the HMA (Figure S48) and SEM with energy dispersive spectroscopy (EDS) of HMA1 and HMA7 was used to do an elemental analysis (Figure S49 and Figure S50). Electron micrographs were recorded on JEOL JSM-6510LV using both secondary and backscatter detectors for imaging and EDS detector for elemental analysis. The surface of BaseResin1 had dust particles due to the tacky nature of the surfaces, while the Antistatic1 surface was clear with no distinguishing features.

S4. Scanning electron microscopy

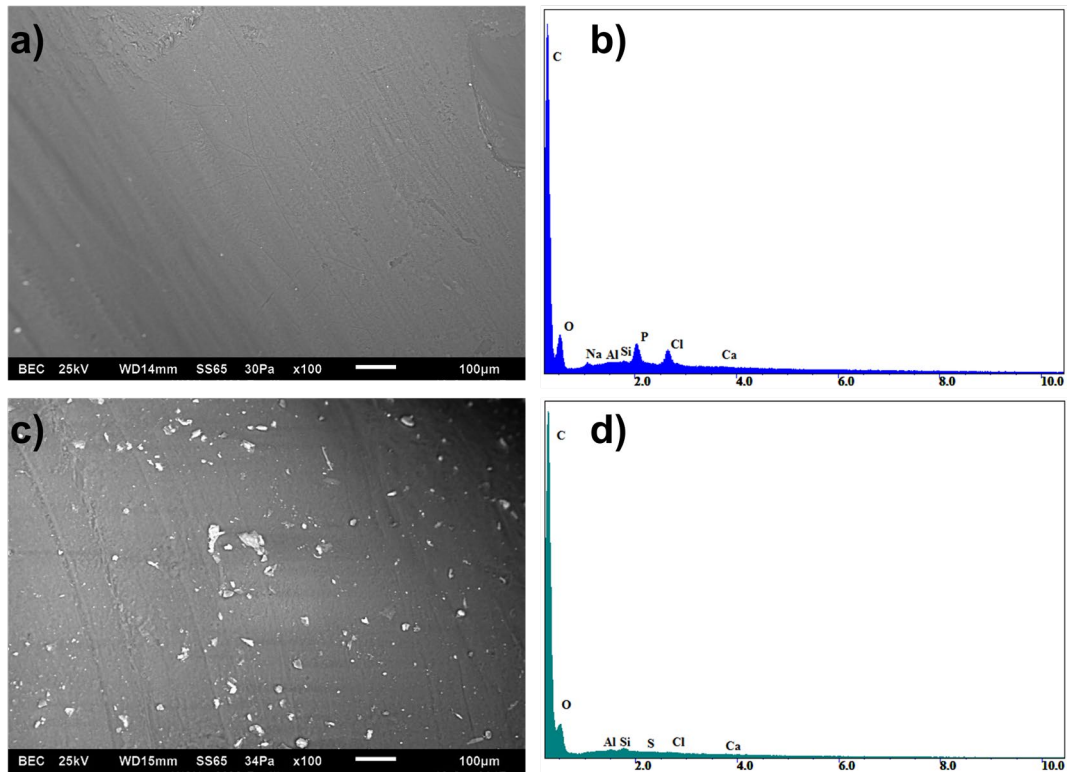


Figure S48: (a and c) SEM image and (b and d) elemental analysis using EDS of (a and b) Antistatic1, and (c and d) BaseResin1.

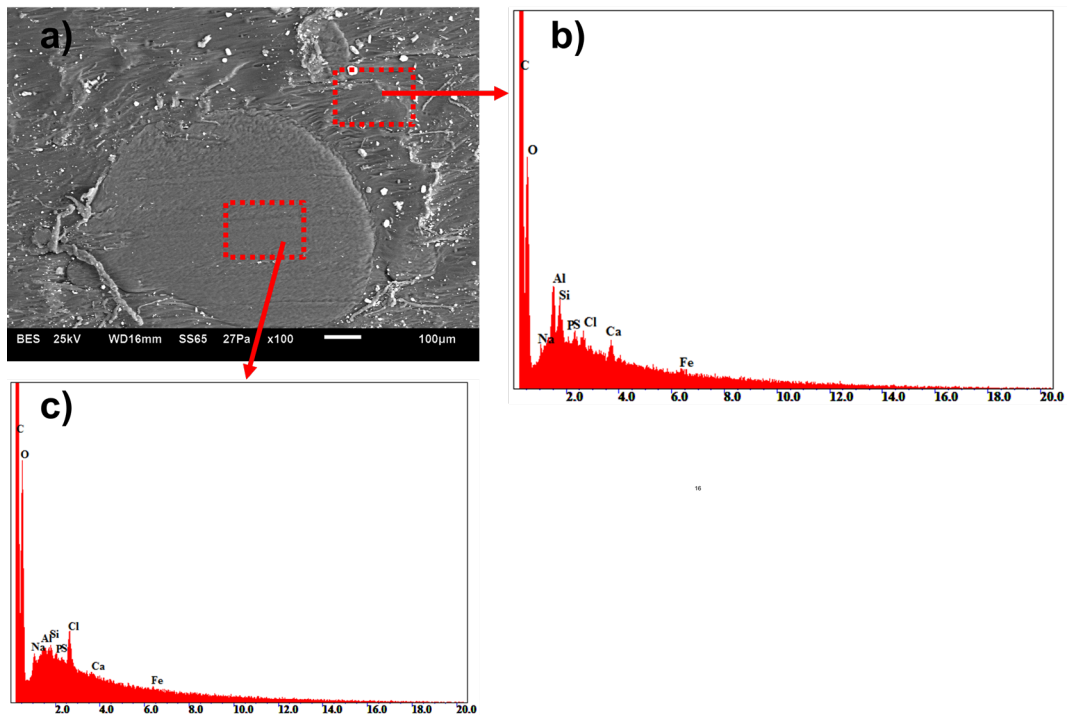


Figure S49: (a) SEM image of HMA1 and elemental analysis using EDS of (b) the HMA matrix and (c) Antistatic1 aggregates.

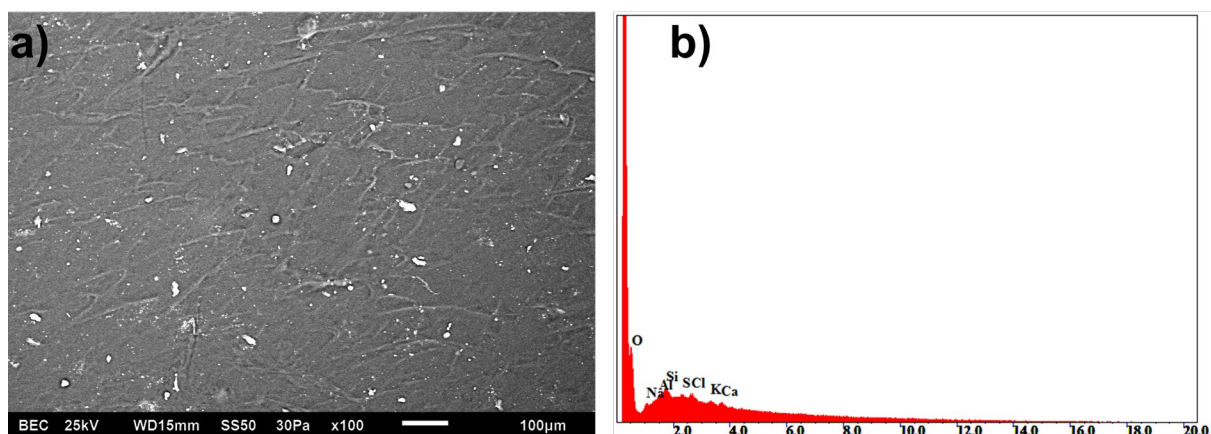


Figure S50: (a) SEM image and (b) elemental analysis using EDS of HMA7.

S5. X-ray diffraction

Table S11: Signal position, corresponding d -spacing, and signal intensity on X-ray diffractograms of Antistatic1, BaseResin1 and HMA1 (Figure 3).

Sample	2θ (°)	d -spacing (nm)	Intensity
Antistatic1	9.7	0.91	Very weak
	21.89	0.41	Very strong
	29.44	0.30	Very weak
	40.83	0.22	Weak
BaseResin1	7.004	1.26	Very weak
	9.648	0.92	Very weak
	20.2	0.44	Very strong
	20.84	0.43	Very weak
	21.69	0.41	Very weak
	29.66	0.30	Very weak
	40.79	0.22	Weak
HMA1	9.688	0.91	Very weak
	20.34	0.44	Very strong
	21.63	0.41	Very weak
	23.93	0.37	Very weak
	40.85	0.22	Weak

S6. Thermogravimetric analysis

Thermogravimetric analysis measurements were conducted on a Netzsch STA449C Jupiter, with 2-6 mg samples in an aluminum crucible, with a 10 °C min⁻¹ ramp from 30 to 590 °C, in air mixture (80 % nitrogen, 20 % oxygen) (Figure S49).

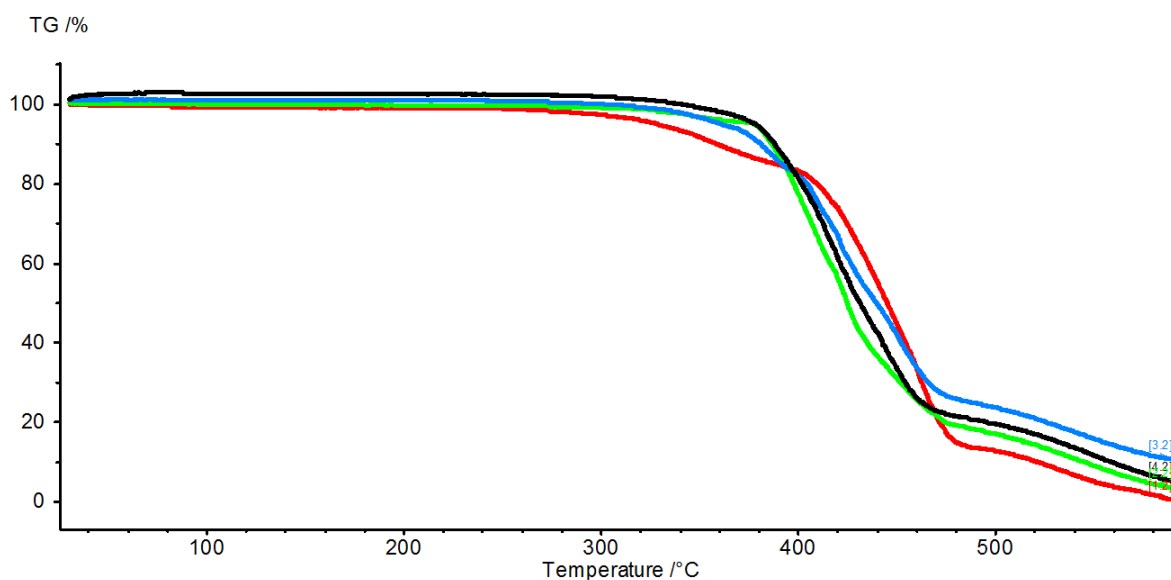


Figure S51: TGA traces of BaseResin1 (green), Antistatic1 (red), HMA2 (blue), and HMA7 (black).

The onset of degradation temperature was determined as the temperature at which 1 % mass loss occurs above 100 °C ($T_d^{0.01}$). The extrapolated onset of degradation temperature (T_d) according to the standard ASTM E2550³⁵ was determined as the point of intersection of the starting-mass baseline and the tangent to the TGA curve at the point of maximum gradient. They are listed together with the mass losses at 100 °C, 200 °C, 250 °C and 300 °C in Table S12.

Table S12: Summary of thermogravimetric analysis of samples.

Sample	$T_d^{0.01}$ (°C)	T_d (°C)	Mass loss (%) at specific temperatures				
			100 °C	200 °C	300 °C	400 °C	500 °C
BaseResin1	312	380	0.3	0.3	0.5	21.7	60.3
Antistatic1	274	403	0.5	0.2	1.8	14.2	70.6
HMA2	299	380	-0.1	0.1	0.9	18.2	58.2
HMA7	305	381	-1.7	0.1	0.7	20.6	61.7

S7. Differential scanning calorimetry

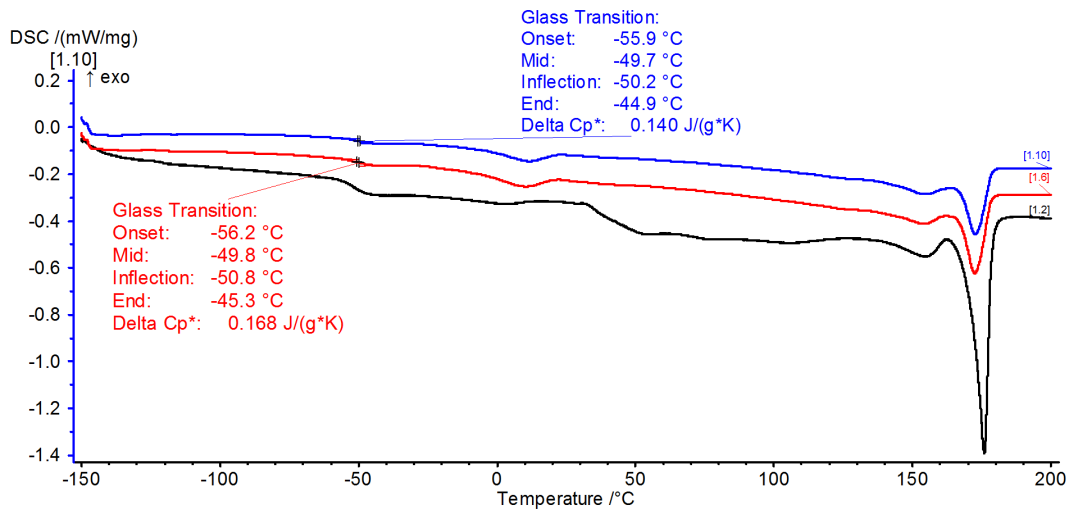


Figure S52: DSC trace of the first (black), second (red), and third heating (blue) along with T_g values for the Antistatic1.

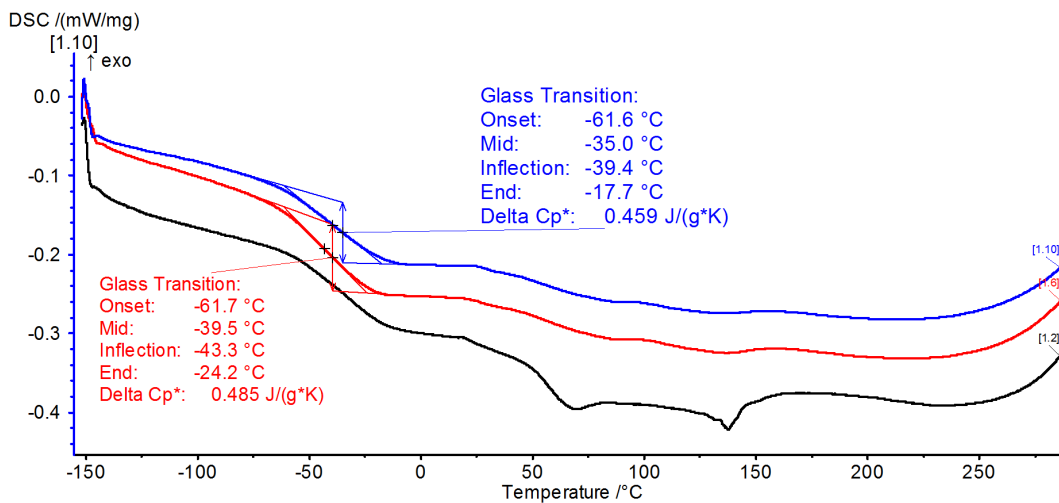


Figure S53: DSC trace of the first (black), second (red), and third heating (blue) along with T_g values for BaseResin1.

S7. Differential scanning calorimetry

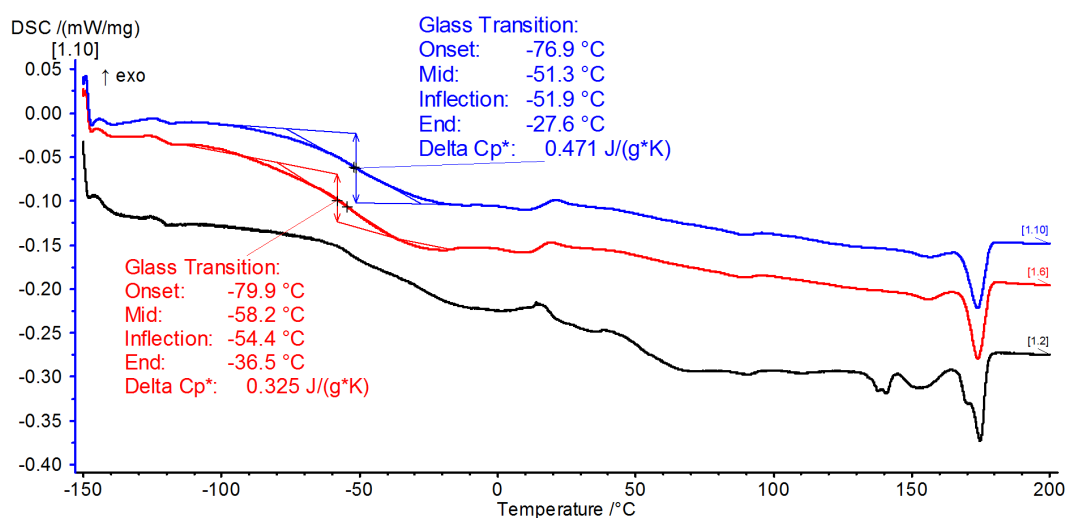


Figure S54: DSC trace of the first (black), second (red), and third heating (blue) along with T_g value for HMA1.

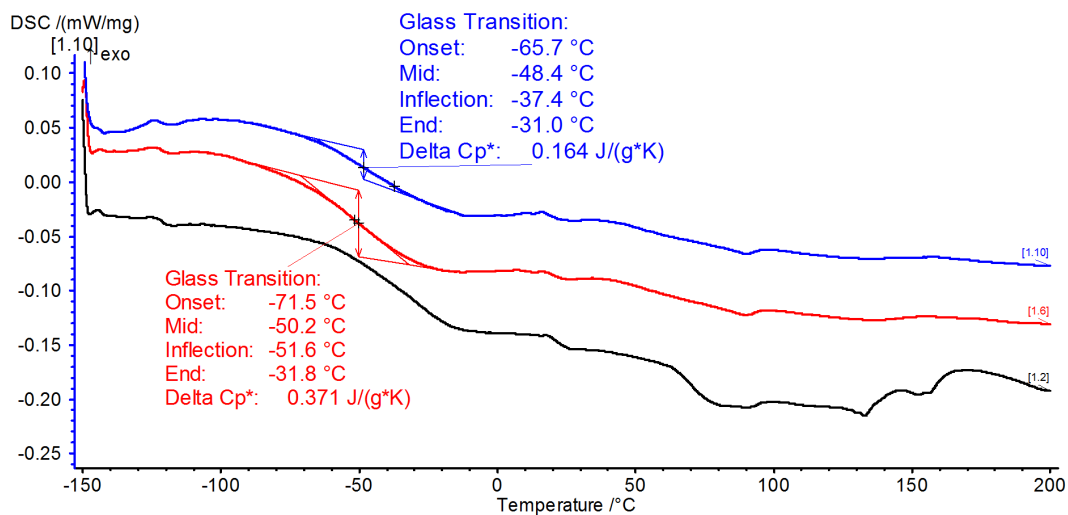


Figure S55: DSC trace of the first (black), second (red), and third heating (blue) along with T_g values for HMA7.

Table S13: Summary of the T_g of Antistatic1, BaseResin1, HMA1, and HMA7.

Sample	T_g (°C)		
	2 nd Heating	3 rd Heating	Average
Antistatic1	-49.8	-49.7	-50
BaseResin1	-39.5	-35	-37
HMA1	-58.2	-51.3	-55
HMA7	-50.2	-48.4	-49

S8. Mechanical and adhesive properties

Table S14: Individual values of Young's modulus, Shore A hardness, and T-peel strength at different temperatures for HMA7.

Temperature (°C)	Young's modulus (MPa)	Shore A hardness	T-peel strength (MPa)
-23	78.2, 45.2, 76.1, 77	92, 95, 92.5, 90, 90.5, 89.5, 87, 87.5, 88.5, 89	
3	12, 6.5, 11.6, 8	80, 80, 86, 87.5, 82, 84, 83.5, 86, 84, 85	
23	8.8, 5, 8.8, 5.4	80, 83, 79.5, 80, 83, 81.5, 81.5, 80.5, 81, 80	4.18
24	8.6, 4.9, 8.7, 5.3		
37	7.6, 4.5, 8, 4	78.5, 81, 79.5, 80, 79.5, 80.5, 80.5, 81, 80.5, 80, 81, 82.5, 82, 82, 80, 82.5, 79.5, 80, 80, 80	
40	7.4, 4.4, 7.8, 3.7		
45	7.2, 4.1, 7.4, 3.4	69.5, 68, 72, 71.5, 74.5, 72.5, 76, 76.5, 70, 76, 78.5, 78.5, 76, 74, 74, 77, 73.5, 77.5, 78, 76	0.88
50	6.7, 3.8, 7, 3.1		
55	5.9, 3.6, 6.4, 3	65.6, 66, 65, 73, 73, 66, 69, 67.5, 68, 64, 68, 69, 70, 70.5, 75, 74.5, 70, 68.5, 69, 69	
60	5.1, 3.4, 5.8, 2.9		
65	4.6, 3.1, 5.2, 2.9	66, 68, 68.5, 70.5, 71, 67, 67.5, 70, 72, 69.5, 69.5, 70, 72, 69, 71.5, 70.5, 65, 66.5, 71, 70	0.37
70	4.2, 4.8		
75	3.9	64.5, 64, 63.5, 66, 65, 67, 64, 66, 65, 66.5, 66.5, 63.5, 64.5, 65, 64.5, 68.5, 68, 67, 67.5, 67	
85		55.5, 56.5, 57.5, 60, 57.5, 56.5, 61, 60, 61.5, 62, 60.5, 60.5, 61, 62, 62.5, 61, 59.5, 61, 62, 62	
95		55, 54, 53, 53.5, 51, 53, 57, 59, 51, 53.5, 54, 53, 53.5, 53, 55, 53, 54.5, 56, 55, 53.5	
105		48.5, 49.5, 51, 51, 53, 47, 48, 52, 53, 52, 50.5, 53, 49, 51, 54, 52, 53, 50.5, 52, 51	
115		36.5, 36.5, 39.5, 36, 37, 39, 37.5, 40.5, 42.5, 40, 41, 42, 43, 43, 41, 44, 43, 41, 39, 39.5	

S8. Mechanical and adhesive properties

Table S15: Shore A hardness values for BaseResin1.

Temperature (°C)	Shore A hardness	Average	Standard deviation
23	79.5, 71, 78, 76, 74, 76, 76, 77, 76.5, 77.5, 78, 81, 76, 80, 78, 75, 75, 75.5, 76	76.6	2.3

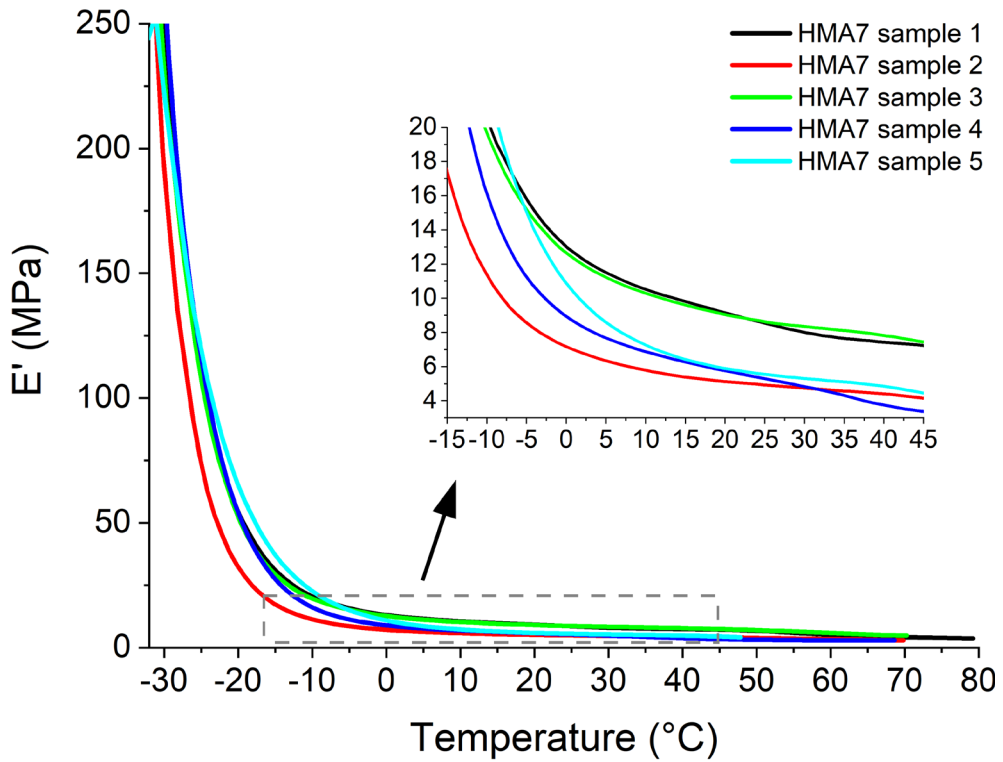


Figure S56: Young's modulus of HMA7 determined using dynamic-thermal analysis via three-point flexural test module.

S8. Mechanical and adhesive properties

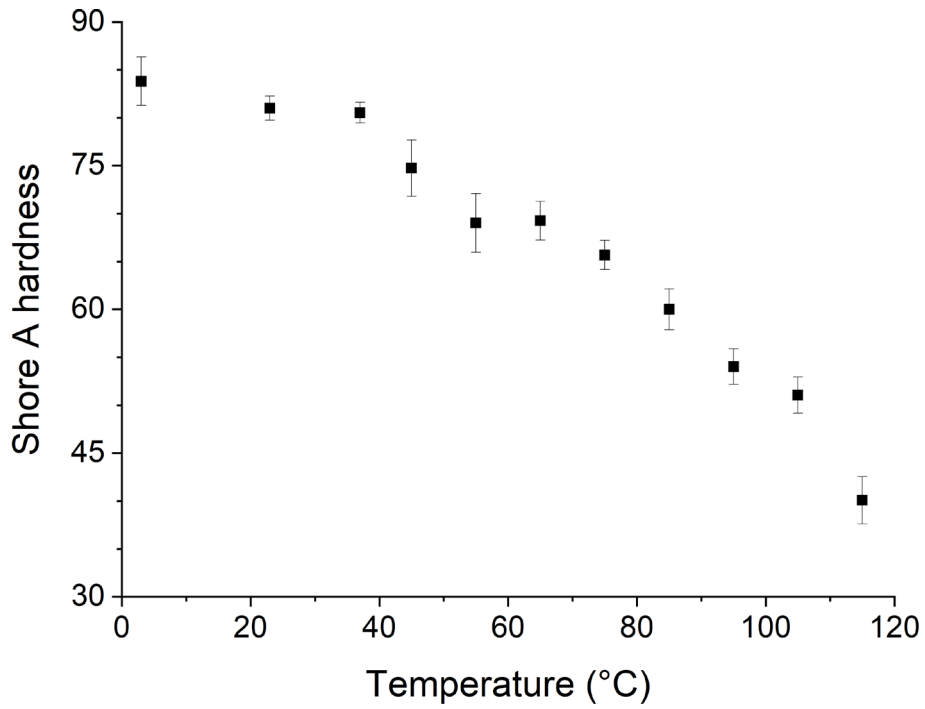


Figure S57: Shore A hardness of HMA7 at different temperatures (error bars represent the standard deviation of 5 measurements).

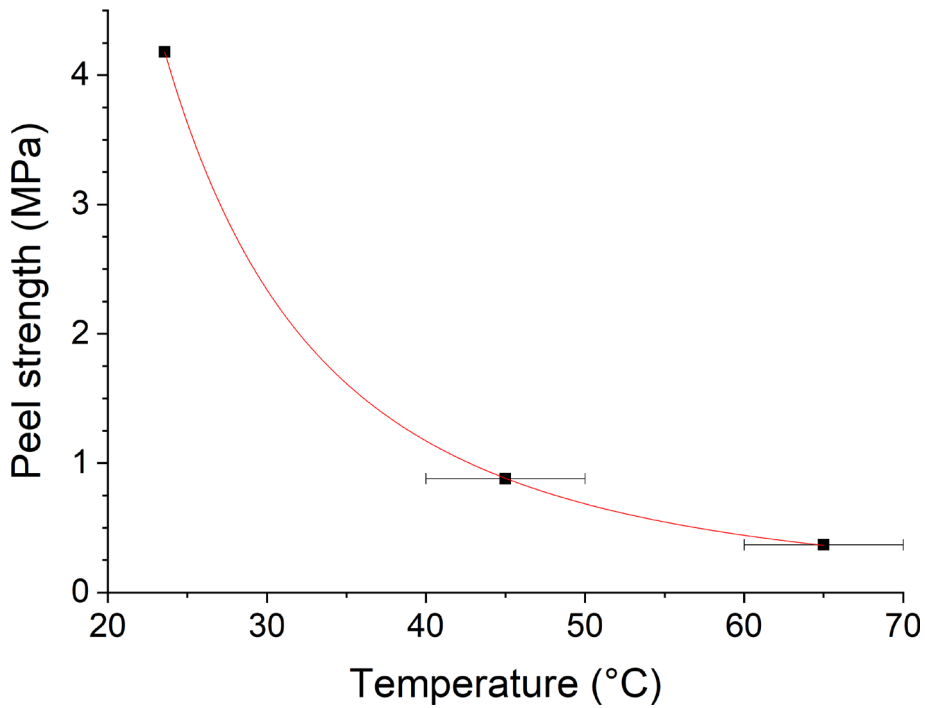


Figure S58: T-peel strength of HMA7 plotted against temperature with power fit ($y=8.83 \cdot 10^3 \cdot x^{-2.4}$, $R^2 = 0.999$) (error bars represent the range of temperature of the measurements).

References

1. S. Krimm, C. Y. Liang and G. B. B. M. Sutherland, *J. Chem. Phys.*, 1956, **25**, 549-562.
2. R. M. Silverstein, F. X. Webster and D. Kiemle, in *Spectrometric Identification of Organic Compounds*, John Wiley & Sons, Inc., Hoboken, New Jersey, USA, 7 edn., 2005, ch. 2, pp. 72-126.
3. E. Hablot, A. Tisserand, M. Bouquey and L. Avérous, *Polym. Degrad. Stabil.*, 2011, **96**, 1097-1103.
4. T. Schadle, B. Pejic and B. Mizaikoff, *Anal. Methods*, 2016, **8**, 756-762.
5. J. Charles, G. R. Ramkumaar, S. Azhagiri and S. Gunasekaran, *E-J. Chem.*, 2009, **6**, 23-33.
6. P. G. Kadam and S. T. Mhaske, *J. Polym. Mater.*, 2013, **30**, 65-78.
7. R. F. Li and X. Z. Hu, *Polym. Degrad. Stabil.*, 1998, **62**, 523-528.
8. T. Kyu, T. I. Chen, H. S. Park and J. L. White, *J. Appl. Polym. Sci.*, 1989, **37**, 201-213.
9. S. A. Idris, O. A. Mkhathresh and F. Heatley, *Polym. Int.*, 2006, **55**, 1040-1048.
10. J. Han, Z. Cao and W. Gao, *J. Mater. Chem. A*, 2013, **1**, 4941-4944.
11. P. G. Kadam and S. T. Mhaske, *Int. J. Adhes. Adhes.*, 2011, **31**, 735-742.
12. B. Mailhot, S. Morlat-Thérias, M. Ouahioune and J.-L. Gardette, *Macromol. Chem. Phys.*, 2005, **206**, 575-584.
13. N. Vasanthan and D. R. Salem, *J. Polym. Sci. Pol. Phys.*, 2001, **39**, 536-547.
14. P. McConville and J. M. Pope, *Polymer*, 2001, **42**, 3559-3568.
15. M. Mortensen, A. K. Thybo, H. C. Bertram, H. J. Andersen and S. B. Engelsens, *J. Agr. Food Chem.*, 2005, **53**, 5976-5981.
16. H. W. Spiess, *Macromolecules*, 2010, **43**, 5479-5491.
17. H. W. Spiess, *Macromolecules*, 2017, **50**, 1761-1777.
18. X. D. Guan and R. E. Stark, *Solid State Nucl. Magn. Res.*, 2010, **38**, 74-76.
19. A. R. Grimmer, A. Kretschmer and V. B. Cajipe, *Magn. Reson. Chem.*, 1997, **35**, 86-90.
20. B. Langer, I. Schnell, H. W. Spiess and A. R. Grimmer, *J. Magn. Reson.*, 1999, **138**, 182-186.
21. S. Antonijevic and G. Bodenhausen, *Angew. Chem. Int. Edit.*, 2005, **44**, 2935-2938.
22. H. D. Campbell, B. L. Rogers and I. G. Young, *Biochemistry*, 1986, **25**, 172-177.
23. H. J. Pan and B. C. Gerstein, *J. Magn. Reson.*, 1991, **92**, 618-619.

S8. Mechanical and adhesive properties

24. C. P. Grey, C. M. Dobson, A. K. Cheetham and R. J. B. Jakeman, *J. Am. Chem. Soc.*, 1989, **111**, 505-511.
25. P. K. Isbester, A. Zalusky, D. H. Lewis, M. C. Douskey, M. J. Pomije, K. R. Mann and E. J. Munson, *Catal Today*, 1999, **49**, 363-375.
26. T. Takahashi, H. Kawashima, H. Sugisawa and T. Baba, *Macromolecules*, 1999, **15**, 119-123.
27. P. A. Beckmann and C. Dybowski, *J. Magn. Reson.*, 2000, **146**, 379-380.
28. L. C. M. Vangorkom, J. M. Hook, M. B. Logan, J. V. Hanna and R. E. Wasylshen, *Magn. Reson. Chem.*, 1995, **33**, 791-795.
29. T. Ding, Q. Y. Liu, R. Shi, M. Tian, H. Yang and L. Q. Zhang, *Polym. Degrad. Stabil.*, 2006, **91**, 733-739.
30. M. R. Krejsa, K. Udipi and J. C. Middleton, *Macromolecules*, 1997, **30**, 4695-4703.
31. B. S. Holmes, W. B. Moniz and R. C. Ferguson, *Macromolecules*, 1982, **15**, 129-132.
32. M. V. Mokeev and V. V. Zuev, *Eur. Polym. J.*, 2015, **71**, 372-379.
33. J. McMurry, in *Organic Chemistry*, Cengage Learning, Boston, Massachusetts, USA, 9 edn., 2011, ch. 13, pp. 386-419.
34. K. Schmidt-Rohr, J. Clauss and H. W. Spiess, *Macromolecules*, 1992, **25**, 3273-3277.
35. ASTM E2550-17, ASTM International: West Conshohocken, PA, USA, 2010.